Excitonic interplay between surface polar III-nitride quantum wells and MoS_2 monolayer

Danxuan Chen,[*,†] Jin Jiang,[‡] Thomas F. K. Weatherley,[†] Jean-François Carlin,[†] Mitali Banerjee,[‡] and Nicolas Grandjean[†]

†*Laboratory of Advanced Semiconductors for Photonics and Electronics (LASPE)*
‡*Laboratory of Quantum Physics (LQP)*
École Polytechnique Fédérale de Lausanne (EPFL), CH-1015 Lausanne, Switzerland

E-mail: danxuan.chen@epfl.ch
Phone: +41 (0)21 693 45 33

arXiv:2308.10687v3 [cond-mat.mes-hall] 4 Sep 2023

Abstract

III-nitride wide bandgap semiconductors exhibit large exciton binding energies, preserving strong excitonic effects at room temperature. On the other hand, semiconducting two-dimensional (2D) materials, including MoS_2, also exhibit strong excitonic effects, attributed to enhanced Coulomb interactions. This study investigates excitonic interactions between surface GaN quantum well (QW) and 2D MoS_2 in van der Waals heterostructures by varying the spacing between these two excitonic systems. Optical property investigation first demonstrates the effective passivation of defect states at the GaN surface through MoS_2 coating. Furthermore, a strong interplay is observed between MoS_2 monolayers and GaN QW excitonic transitions. This highlights the interest of the 2D material/III-nitride QW system to study near-field interactions, such as Förster resonance energy transfer, which could open up novel optoelectronic devices based on such hybrid excitonic structures.

Keywords

MoS_2, GaN, surface quantum wells, cathodoluminescence, FRET

Introduction

Since the breakthroughs of blue light-emitting diodes (LEDs) in the 1990s,[1] III-nitrides have emerged as a major family of contemporary semiconductors. This development is attributed to their remarkable optoelectronic properties, including a direct bandgap spanning from the near infrared to the deep ultraviolet, thermal and chemical robustness, and large exciton binding energies,[2] which ensures strong excitonic effects,[3] with for instance, the achievement of room temperature (RT) polariton lasing.[4]

The isolation of graphene in 2004[5] marked the inception of a new era in solid-state physics. Owing to the weak interlayer van der Waals (vdW) interactions, layered materials can be easily exfoliated into atomically thin layers, i.e., two-dimensional (2D) materials, and seamlessly integrated with other materials, granting notable flexibility in constructing vdW heterostructures. Among various 2D materials, semiconducting transition-metal dichalcogenides (TMDs), such as MoS_2, exhibit a sizeable bandgap[6] and strong light-matter coupling,[7] making them highly desirable for optoelectronic applications. When the layer thickness is reduced to the atomic scale, carriers in 2D TMDs exhibit excitons with binding energies typically one to two orders of mag-

nitude larger than those observed in conventional semiconductors,[8] which ensures robust excitonic features at RT.[9]

Mixed-dimensional vdW heterostructures combining TMDs with III-nitrides have already been proposed for a diverse range of applications including LEDs,[10] water splitting,[11] and photodetection.[12] In such heterostructures, III-nitrides are typically utilized in bulk form. A closer look at TMD/III-nitride interactions requires the study of the exitonic interplay at the vdW interface only. However, conventional semiconductor surfaces possess deep states in the bandgap which act as non-radiative recombination centers (NRCs). These NRCs can effectively suppress excitonic features near the surface.[13] In contrast to other III-V semiconductors, III-nitrides exhibit relatively low surface recombination velocity.[14] In addition, by carefully designing the quantum well (QW) structure, the exciton binding energies can be further increased compared to those in bulk materials.[15] Moreover, wurtzite III-nitrides exhibit large polarization mismatches at heterointerfaces,[16] which results in a strong built-in electric field in the well and thereby large electron-hole dipoles in the QW. Then, 2D TMD excitons in their vicinity should enable dipole-dipole coupling, known as Förster resonance energy transfer (FRET).[17] This effect has been observed between CdSe/ZnS nanocrystals and surface InGaN QWs and could be utilized for developing highly efficient "energy-transfer color converters".[18]

In this study, we tune the excitonic interaction between 2D MoS_2 and surface polar GaN/AlGaN QWs by varying the distance, d, between the two. Cathodoluminescence (CL) measurements on bare QWs show appreciable emission at RT even in the absence of a surface barrier, which confirms a low surface recombination rate. Upon coating the surface with MoS_2, the CL intensity markedly changes, indicating that deep traps still exist at the surface and are passivated by the MoS_2 coating. Eventually, CL results from the sample with d = 15 nm unveil a pronounced change of the emission at QW excitonic transitions upon monolayer (ML)-MoS_2 deposition. This phenomenon points out the role of FRET between ML-MoS_2 and surface GaN QW.

Results and Discussion

The sample structure of c-axis oriented surface GaN/AlGaN QWs is illustrated in Fig. 1**(a)**. The well thickness of 3 nm is chosen as a compromise between maximizing the binding energy and maintaining the dipolar nature of excitons.[15] The sample without the AlGaN surface barrier is considered a "QW" with d = 0 nm. A 500 nm thick AlGaN spacer is inserted beneath the QW to prevent electron-beam-generated carriers from reaching the buffer where they could give rise to parasitic luminescence (Supporting Information (SI) Sec. 2). The CL spectra of surface QWs are presented in Fig. 1**(b)**, with dominant peaks at $\sim$ 3.43 eV and $\sim$ 3.63 eV, attributed to the GaN QWs and AlGaN spacers, respectively. The first important observation is that, in contrast to near-surface GaAs QWs,[13] all present GaN QWs exhibit a strong emission at RT, even in the absence of a surface barrier (SI Sec. 3).

Now we will delve into the characteristics of each CL peak. As the thickness of the surface barriers is smaller than the carrier diffusion length in $Al_{0.1}Ga_{0.9}N$,[19] it is reasonable to assume that most of the carriers generated in the surface barrier diffuse to the QW where they recombine. Hence, the AlGaN emission in Fig. 1**(b)** originates from the spacer that is farther away from the surface, where carriers recombine before reaching the QW. The depth of the interaction volume of the 5 keV electron beam in these samples is more than 100 nm (SI Sec. 2), which implies that the total carrier generation rate remains nearly constant regardless of the position of the QW in the surface region, i.e., d. This is corroborated by the comparable AlGaN peak intensity in all samples (SI Sec. 3). On the other hand, the GaN QW peak changes markedly with d. In contrast to other surface QWs, the peak of the uncapped well (d = 0 nm) blueshifts by $\sim$ 30 meV. This can be explained by a stronger carrier quan-

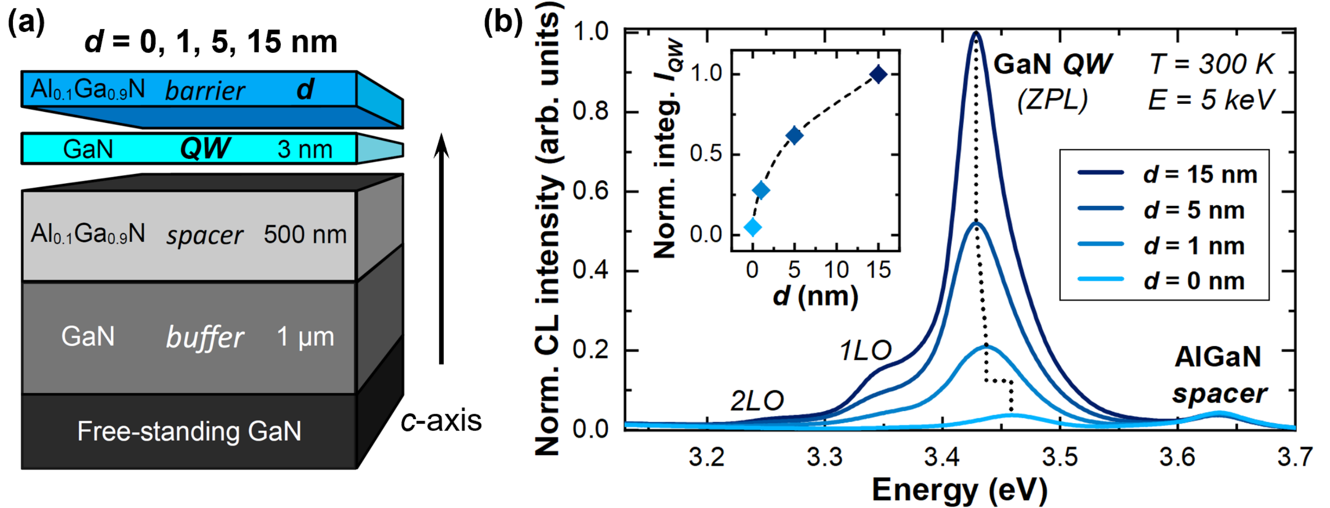

Figure 1: **(a)** Sample structure of surface QWs and **(b)** corresponding CL spectra acquired at 300 K under an electron beam energy of 5 keV. In the inset, the integrated QW intensity (I_{QW}), including the zero-phonon line (ZPL) and its longitudinal optical (LO) phonon replicas, is plotted as a function of surface barrier thickness (d). The intensity error bars are not visible in the plot as they are smaller than the size of the diamond symbol used.

tum confinement imposed by the free surface (SI Sec. 3). The integrated QW intensity (see SI Sec. 3 for calculation details) in Fig. 1**(b)** exhibits a nonlinear increase with increasing d, which indicates a reduction of non-radiative recombination channels. For a c-plane (Al)GaN surface, a high density of deep levels can act as effective NRCs.[20] Thus, carriers in surface QWs can tunnel through the nanoscale barrier and be captured by surface traps (STs). The d-dependent QW intensity can be modeled by an exponential function to account for carrier tunneling[13] (SI Sec. 3). Therefore, the nonlinear increase in QW emission with increasing d demonstrates the significant impact of STs on surface GaN QWs, despite the typically low surface recombination velocity usually ascribed to III-nitrides. This highlights the importance of surface passivation for III-nitrides, particularly in devices with a high surface-to-volume ratio.[21]

Mechanically exfoliated MoS_2 flakes were prepared on a SiO_2/Si substrate, where the contrast in an optical microscope is highly sensitive to MoS_2 thickness due to light interference[22] (Figs. 2**(a, d)**). After precise characterization of the layer thickness (SI Sec. 4), the selected flakes were deposited on the surface GaN QWs. Hyperspectral CL maps were acquired on the MoS_2 flake regions. Each pixel in the map corresponds to the CL at that position and the associated spectrum was fitted to generate integrated intensity maps of the GaN QW and AlGaN emissions (SI Sec. 5). To facilitate the comparison, all intensity maps were normalized by the average intensity of the background (SI Sec. 5).

Among all intensity maps, the uncapped GaN QW ($d = 0$ nm) shows a peculiar behavior: the region covered by MoS_2 exhibits a strongly enhanced emission (Fig. 2**(b)**). This is not consistent with the high spectral absorptance of MoS_2 in the range of (Al)GaN emission ($\sim$ 10% of the incident light is absorbed by ML-MoS_2).[23] In contrast, the AlGaN intensity map extracted from the same sample shows a decrease in intensity with increasing MoS_2 thickness (Fig. 2**(c)**), as expected from absorption.[24] Additionally, when the GaN QW is slightly moved away from the surface, i.e., $d = 1$ nm, its CL intensity is also reduced with the presence of MoS_2 (Fig. 2**(e)**). It is noteworthy that, despite similar MoS_2 spectral absorptance in the corresponding energy ranges, the contrast observed from the GaN QW with $d = 1$ nm differs from that of the AlGaN emission (Fig. 2**(c)**). The former shows a more pronounced reduction in

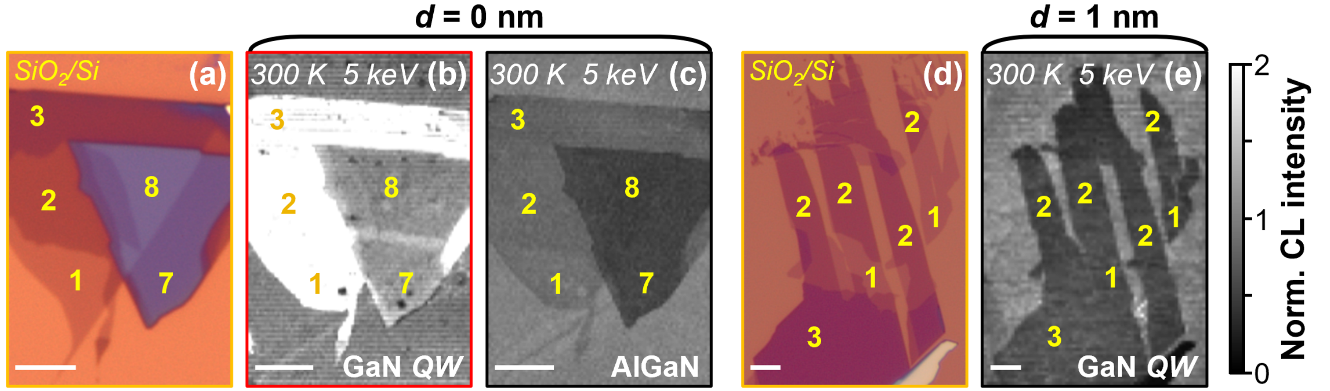

Figure 2: **(a, d)** Optical micrographs of the selected MoS_2 flakes on a SiO_2/Si substrate. Normalized integrated CL intensity maps of the **(b)** GaN QW and **(c)** AlGaN emissions from the uncapped GaN QW ($d = 0$ nm), as well as **(e)** the GaN QW emission from the sample with $d = 1$ nm, acquired with an electron beam energy of 5 keV at 300 K. For each map, the normalization was performed using the average intensity in the region without MoS_2. All CL maps are plotted on an intensity scale of $0-2$. The numbers in yellow indicate the number of MoS_2 MLs in the corresponding region. Scale bars correspond to a length of 5 μm.

intensity throughout the entire region covered by MoS_2 of $1-3$ MLs. The underlying reason will be elucidated later. On the other hand, considering the abnormal increase in CL intensity linked to MoS_2 for the uncapped QW, it is evident that only the emission of the layer in direct contact with the MoS_2 flake is enhanced, indicating that the MoS_2-enhanced GaN emission is associated with surface passivation.

To confirm this hypothesis, we performed CL experiments on a GaN epilayer coated by MoS_2 (SI Sec. 6). The CL map also exhibits an increase in GaN emission in the presence of MoS_2, albeit weaker compared to the case of the uncapped GaN QW. This is consistent with a surface passivation effect: in a GaN epilayer, CL emission comes from both the surface and bulk regions, which diminishes the surface impact.

In order to obtain more quantitative information from the results of the uncapped QW, average CL spectra were extracted from regions with different MoS_2 thicknesses (SI Sec. 5), as shown in Fig. 3**(a)**. These spectra were deconvoluted to derive the integrated intensities of the GaN QW and AlGaN spacer peaks, respectively (SI Sec. 3). Let us consider first the AlGaN spacer emission, which is not affected by any surface effects (Fig. 3**(b)**). It exhibits a monotonic decrease with increasing MoS_2 thickness, as expected from absorption. It is important to note that the presence of MoS_2 has a negligible impact on carrier injection into the samples, primarily due to the limited interaction of the electron beam with these ultra-thin layers.[25] To model the AlGaN intensity decrease, we consider that the interlayer coupling in MoS_2 does not strongly influence the absorption, thus the absorption in each ML is nearly the same. Therefore, the normalized intensity can be fitted with a power function: $I(n) = (1-a)^n$, where n is the number of MoS_2 MLs and a is the absorptance in each ML. The fit gives $a \approx 10\%$, which agrees with the absorptance measured in ML-MoS_2 at 3.63 eV,[23] i.e., the peak energy of AlGaN emission. Similarly, Fig. 3**(c)** shows the plot of the GaN QW CL intensity as a function of MoS_2 thickness. Fitting the data with the same absorption model reproduces the overall trend, with $a \approx 10\%$, matching ML-MoS_2 absorptance at 3.45 eV.[23] However, this fit does not capture the experimental data at $n = 0$, instead predicting an intensity 3.6 times higher than the measured value. This indicates that the deposition of the first ML-MoS_2 results in a strong increase in the surface emission, i.e., the emission of the uncapped QW, due to single ML-MoS_2 surface passivation effect.

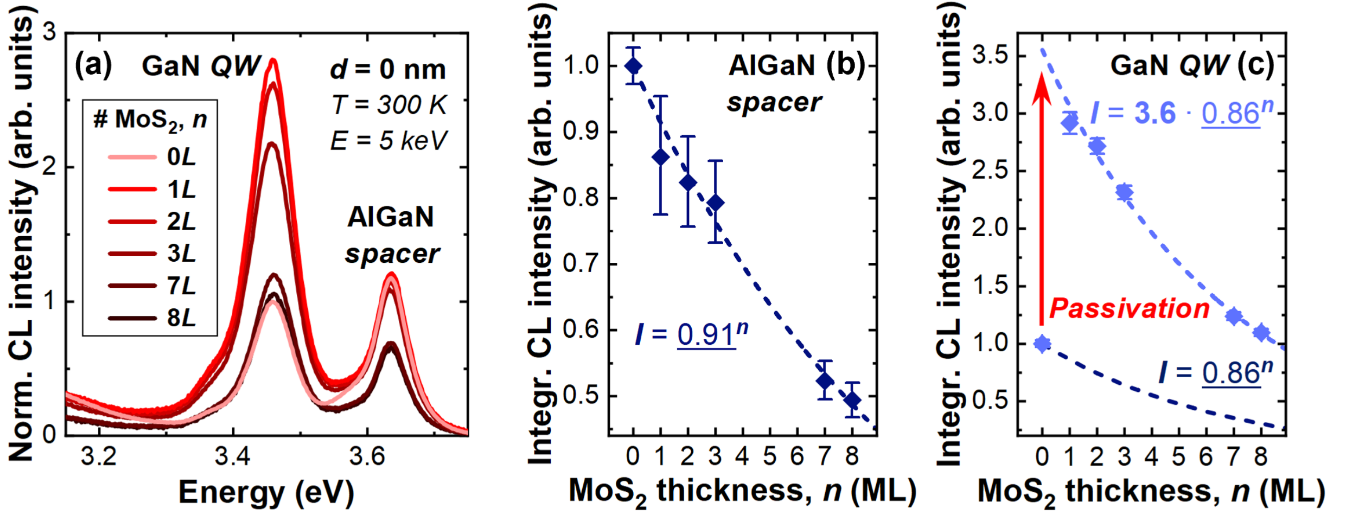

Figure 3: **(a)** Average RT CL spectra collected from the uncapped GaN QW ($d = 0$ nm) in areas with varying MoS_2 thickness, represented by the number of MLs (n). All spectra are normalized to the peak intensity of the GaN QW emission in the region without MoS_2 ($0L$). Normalized integrated CL intensity as a function of MoS_2 thickness for **(b)** the AlGaN spacer emission and **(c)** the GaN QW emission. The dashed lines represent the fit assuming the same absorption in each ML-MoS_2, with the corresponding expression next to them. Some intensity error bars are not visible in the plots as they are smaller than the size of the diamond symbol used.

A possible explanation for surface passivation is based on type-II band alignment between MoS_2 and GaN:[12] the unintentionally doped GaN surface exhibits an upward surface band bending due to the presence of STs (Fig. 4**(a)**); with MoS_2 deposited on the surface, charge transfer between the two materials leads to an upward band bending in MoS_2 and a downward band bending in GaN (Fig. 4**(b)**). Consequently, STs are occupied and are no longer capable of trapping excitons in the surface region, therefore, surface emission is markedly enhanced.

As the deposition of MoS_2 exerts a significant impact on the emission of the uncapped QW, it is not a suitable sample for studying excitonic interplay between the two materials. Conversely, in the sample with $d = 15$ nm, carriers confined in the well are no longer interacting with STs (SI Sec. 3), making this system ideal for gaining insight into the excitonic interactions. The CL spectra with different MoS_2 thicknesses are displayed in Fig. 5**(a)**. Throughout the entire detection range, from ~ 3.0 eV to ~ 3.7 eV, the CL intensity decreases with increasing MoS_2 thickness. This energy range coincides with the C-absorption band of ML-MoS_2.[23] Interestingly, for all peaks related to the GaN QW emission, including the ZPL and its LO phonon replicas, the intensity difference between ML-MoS_2 capped QW ($1L$) and bare QW ($0L$) is notably larger than the intensity change observed when increasing the MoS_2 thickness by 1 ML.

To get a deeper insight into the influence of MoS_2 on the QW emission, we computed the intensity contrast, following the formula:

$$\text{Contrast}[(n+1)L\text{-to-}nL](E) = 1 - \frac{I_{(n+1)L}(E)}{I_{nL}(E)}$$

where I_{nL} is the CL intensity of the region covered by nL-MoS_2, i.e., MoS_2 of n MLs, as a function of photon energy, E. As depicted in Fig. 5**(b)**, the intensity contrast between regions covered by $4L$- and $5L$-MoS_2 (light grey curve) aligns with the reported ML-MoS_2 spectral absorptance[23] (black dashed curve). On the contrary, the contrast between the background and the $1L$-MoS_2 region (dark grey curve) exhibits a significant discrepancy in the emission range of GaN QW and AlGaN. In the range around the AlGaN bandgap, a peak

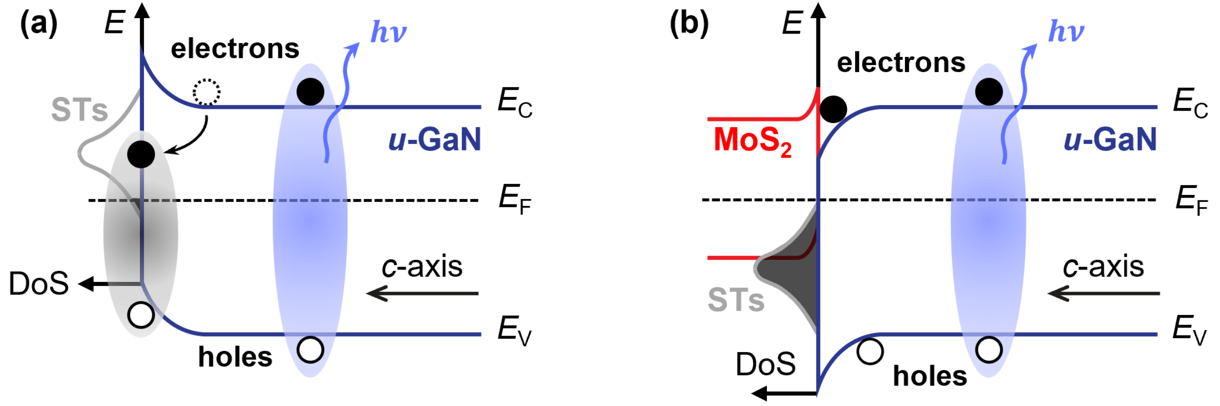

Figure 4: Surface band bending of **(a)** bare unintentionally doped GaN (u-GaN) and **(b)** u-GaN coated with MoS_2 after interfacial charge transfer.[12] The density of states (DoS) of surface traps (STs) in u-GaN is depicted in both situations, with the black shaded part representing occupied states. The grey ellipse represents an exciton captured by a ST and does not emit light, while the blue ellipses represent free excitons that can emit light through radiative recombination.

with a negative contrast is observed, i.e., higher AlGaN emission in the presence of ML-MoS_2. This can be explained by the surface passivation induced by ML-MoS_2, which enhances surface emission from the AlGaN barrier (SI Sec. 7). In the range of GaN QW emission, multiple peaks, with contrasts much higher than expected from absorptance only, are observed. The dominant peak at 3.41 eV, along with the two lower-energy peaks, can be associated with the ZPL and the corresponding LO phonon replicas of the GaN QW emission in the CL spectrum (light red curve). The carrier density in the well is on the order of 10^{12} cm^{-2} (SI Sec. 2). This is close to the critical carrier density of the Mott transition reported for similar GaN QWs.[26,27] Therefore, CL peaks of the GaN QW can arise from two possible physical origins: excitonic transitions or electron-hole plasma emission. The presence of excitonic features in the well can be confirmed by the energy spacing between adjacent peaks of the QW emission. Theoretically, the peak emission energy of the mth LO phonon replica of excitons can be expressed as:[28]

$$\begin{aligned} E_m &= E_0 - mE_{\text{LO}} + E_{\text{kin}} \\ &= E_0 - mE_{\text{LO}} + \frac{D}{2}k_BT \end{aligned}$$

where E_0 is the peak energy of the ZPL, E_{LO} is the LO phonon energy (92 meV for GaN[29]), and E_{kin} is the kinetic energy of the excitons, which depends on D, the dimensionality of the system ($D = 2$ for excitons confined in a QW). T is the lattice temperature, and k_B is the Boltzmann constant. For excitonic emission from a GaN/AlGaN QW at 300 K, the theoretical energy spacing between the ZPL and the 1$^{\text{st}}$ LO phonon replica should be $E_{\text{LO}} - k_BT$, i.e., 66 meV, whereas the energy spacing between the 1$^{\text{st}}$ and 2$^{\text{nd}}$ LO phonon replicas should be E_{LO}, i.e., 92 meV. This agrees perfectly with the CL spectra shown in Fig. 5**(b)**, which confirms the excitonic nature of the QW emission. Furthermore, the CL emission profile of the GaN QWs is compared to the emission measured by photoluminescence (PL) using a continuous wave (cw) 325 nm laser with a power density of $\sim$ 16 W/cm^2, which results in much lower carrier injection into the QWs (SI Sec. 3). Although the energy peak blueshifts in CL, which may be attributed to the screening of the built-in field at higher carrier density, the line shape remains nearly unchanged. This observation excludes Fermi filling of continuum states, characterized by a strong extension of the high-energy tail, which is typically observed beyond the Mott transition.[26] Therefore, our findings demonstrate that, besides the conventional absorption, there is an additional energy transfer channel between the GaN QW and ML-MoS_2, in resonance with the excitonic transitions in

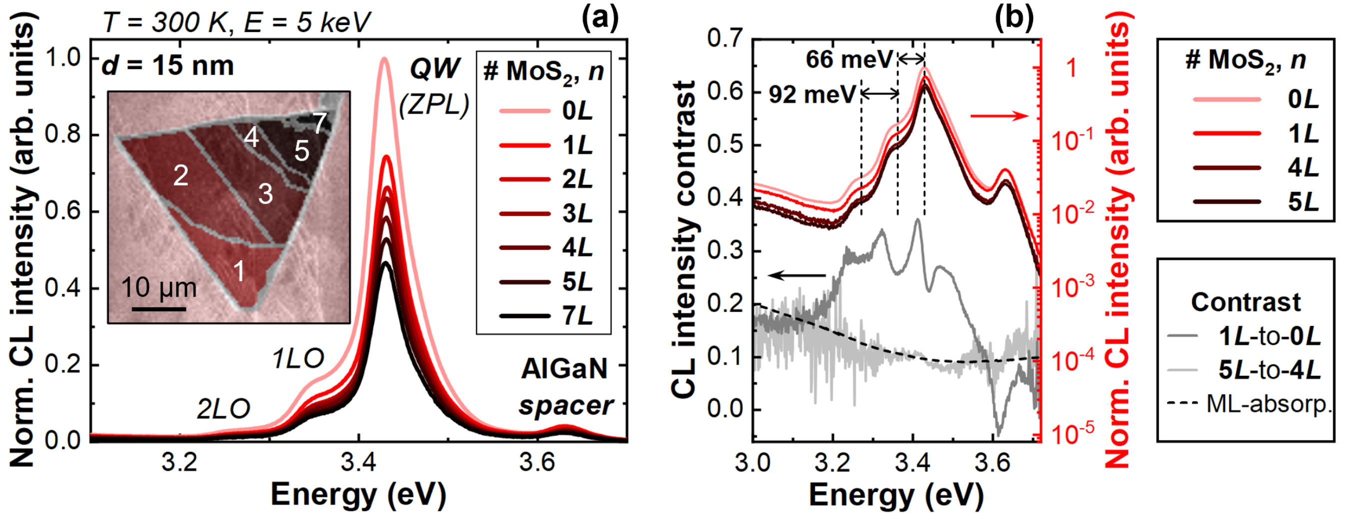

Figure 5: **(a)** Average RT CL spectra taken on the sample with $d = 15$ nm in regions with different MoS_2 thicknesses. The corresponding regions are shown in the inset. **(b)** Intensity contrast between the background ($0L$) and $1L$-MoS_2 region, and contrast between the $4L$- and $5L$-MoS_2 regions, in comparison to the reported ML-MoS_2 spectral absorptance.[23] The related CL spectra are plotted to illustrate the energy range of different emissions.

the QW. Such an effect is clearly observed in the contrast induced by the direct deposition of ML-MoS_2 on the QW surface.

The relevant mechanism is probably FRET, which provides an efficient energy transfer between energy "donor" and "acceptor" materials through non-radiative dipole–dipole coupling.[17] In our case, carriers confined in the polar GaN/AlGaN QW are subjected to a built-in field, forming dipoles which act as energy "donors". On the other hand, different from excitons in other MoS_2 layers, excitons in the ML-MoS_2 on the surface are the closest to the QW dipoles and experience a weaker dielectric screening due to the absence of a layer on top. Furthermore, since the AlGaN surface barrier possesses a polar nature as all III-nitride layers grown along the c-axis, it can enhance the dipolar characteristics of the excitons in direct contact with it. All these result in strong dipoles in ML-MoS_2, which act as energy "acceptors". The associated donor-acceptor distance (d_{DA}) is $\sim$ 15 nm, which is on the order of the typical range for FRET.[30–32] Therefore, we attribute the observed sharp peaks with intensity contrasts as high as $\sim$ 36% to the strong dipolar coupling between excitons in the QW and in ML-MoS_2 in the near-field regime. This effect also explains the difference in CL contrast between the AlGaN emission from the uncapped QW (Fig. 2**(c)**) and the GaN QW emission from the sample with $d = 1$ nm (Fig. 2**(e)**). Specifically, the AlGaN emission originates from the bulk region where the excitonic feature is weaker and d_{DA} is larger. In contrast, the GaN QW emission with $d = 1$ nm is associated with strong excitonic effect in the well, localized very close to MoS_2. As a result, a significant quenching of the emission is observed due to efficient FRET. The peak QW intensity contrast induced by ML-MoS_2 on the sample with $d = 1$ nm is $\sim$ 52% (SI Sec. 8), much higher than the 36% observed for $d = 15$ nm. This difference is consistent with the strong dependence of FRET on d_{DA}. It is important to note that with a thin surface barrier of 1 nm, the QW emission is still strongly influenced by STs (SI Sec. 3). The deposition of ML-MoS_2 should simultaneously cause a negative contrast due to surface passivation. Therefore, the 52% contrast deduced from CL measurements is likely underestimated.

Conclusion

In summary, we investigated the optical properties of a series of surface GaN/AlGaN QWs with variable nanometer-scale surface barrier thickness, $d = 0$ to 15 nm. Thanks to the low surface recombination rate, high CL intensity was observed, even from the uncapped QW ($d = 0$ nm). The QW intensity increased nonlinearly with increasing d, showing the non-negligible impact of deep traps existing at III-nitride surfaces. Using these surface GaN QWs as substrates, we deposited MoS_2 flakes of a few MLs. The presence of MoS_2 enhanced the emission from the uncapped QW, demonstrating III-nitride surface passivation using 2D material coating. For the QW with $d = 15$ nm, unaffected by STs, a strong excitonic interaction between the GaN QW and ML-MoS_2 is observed. This effect is attributed to a strong dipole-dipole coupling, i.e., FRET, between the excitons of the two materials. Our results highlight the potential of surface III-nitride QWs as a platform for investigating the near-field interplay between 2D materials and III-nitrides, which could be applied to develop novel optoelectronics based on such hybrid heterostructures.

Supporting Information

The Supporting Information accompanies this paper. Further details on:

1. Experimental methods
2. Carrier injection in CL
3. Optical properties of surface GaN QWs
4. MoS_2 thickness determination
5. CL data processing
6. MoS_2 on bulk GaN epilayer
7. MoS_2 on GaN QW, $d = 15$ nm
8. MoS_2 on GaN QWs, $d = 1, 5$ nm

Acknowledgement The authors thank Dr. R. Butté (EPFL) for useful discussions. The Interdisciplinary Centre for Electron Microscopy (CIME) at EPFL is acknowledged for access to its facilities. M. B. acknowledges the support of SNSF Eccellenza grant No. PCEGP2_194528, and support from the QuantERA II Programme that has received funding from the European Union's Horizon 2020 research and innovation program under Grant Agreement No. 101017733.

SUPPORTING INFORMATION

1. Experimental methods

Sample growth. The samples used in this study were grown by metalorganic vapor phase epitaxy in a horizontal Aixtron 200/4 RF-S reactor on commercial *c*-plane free-standing GaN substrates with very low dislocation density, typically a few 10^6 cm^{-2}. The growth process can be divided into two parts. First, a rapid growth of the GaN buffer and a $\sim$ 500 nm $Al_{0.1}Ga_{0.9}N$ spacer is conducted at a growth rate of $\sim$ 2 μm/h and a temperature of 1000 °C. Trimethylgallium and trimethylaluminum are used as precursors, and H_2 is used as carrier gas. Then, the growth rate is lowered to 60 nm/h at a temperature of 800 °C for the single QW region, which includes a 5 nm $Al_{0.1}Ga_{0.9}N$ barrier, the 3 nm GaN QW layer, and the $Al_{0.1}Ga_{0.9}N$ surface barrier. This low-temperature (LT) growth is intended to mitigate large-scale Al content fluctuations within the barriers, thereby minimizing the inhomogeneous broadening of the QW emission.[33] For the LT growth, the metalorganic source for gallium is changed to triethylgallium, and the carrier gas is switched to N_2. The entire structure is grown without any intentional doping.

Fabrication of MoS_2-on-(Al)GaN heterostructures. The MoS_2 flakes were obtained through the well-known "scotch-tape" mechanical exfoliation method[5] and deposited on a 10-minute oxygen-plasma-etched SiO_2/Si substrate. The precise thickness of the selected MoS_2 flakes was determined by optical microscopy, atomic force microscopy (AFM) and Raman spectroscopy (SI Sec. 4). Following the characterization, the selected flakes were picked up and transferred onto the cleaned surface of the (Al)GaN samples (QWs and a bulk GaN epilayer) using a dry transfer technique.[34,35] Initially, a high-quality uniform stack of poly(bisphenol A carbonate)/polydimethylsiloxane was prepared on a glass slide. This stack was then mounted on a home-made transfer stage to pick up MoS_2 at 70 °C. Subsequently, the MoS_2 flake was transferred to the surface of the (Al)GaN sample at 150 °C. Finally, the entire sample was immersed in chloroform to clean its surface.

Cathodoluminescence spectroscopy. CL imaging was conducted using a specialized scanning electron microscope system (Attolight Rosa 4634) with an acceleration voltage of 5 kV. A Cassegrain reflective objective was employed to collect the emitted light, which was subsequently directed to

a spectrometer equipped with a 600 lines per mm grating with a blaze wavelength of 300 nm. The dispersed light was then captured by a cooled charge-coupled device camera, enabling the recording of a full intensity-energy spectrum at each pixel, i.e., hyperspectral imaging.

2. Estimation of the carrier density in the QWs

The interaction volume of a 5 keV electron beam at 300 K in bulk $Al_{0.1}Ga_{0.9}N$ is determined through Monte Carlo simulation (*CASINO*),[36] as depicted in Fig. S1**(a)**. For this simulation, an electron beam containing 1×10^6 electrons was used, with a spot size of 25 nm, and an accelerating voltage of 5 kV. This can be deemed representative of all the samples examined in this study, as the thickness of the GaN QW is negligible compared to the overall interaction volume, and a 10% variation in Al content leads to less than 5% change in mass density. Based on the simulation, the normalized energy deposited in the sample is plotted as a function of depth from the surface (Fig. S1**(b)**), which indicates that most of the beam energy is absorbed within a 150 nm region from the surface. Considering that the minority carrier diffusion length in GaN and $Al_{0.1}Ga_{0.9}N$ is typically limited to 100 nm at RT,[19,37] the 500 nm thick $Al_{0.1}Ga_{0.9}N$ spacer serves as an effective barrier which prevents beam-generated carriers from reaching the GaN buffer. Consequently, the observed GaN emission in all the samples is attributed solely to the GaN QWs.

To estimate the carrier density in the QWs (n_{QW}), we first compute the lateral carrier generation rate distribution $F(r)$, where r represents the lateral distance to the beam center using cylindrical coordinates. This is achieved by convolving the carrier generation rate distribution $F_0(r)$, deduced from the simulation, with a Gaussian distribution $G(r)$. Specifically, $F_0(r)$ is obtained by summing the deposited energy over the z direction, assuming that all carriers relax to the QW. $G(r)$ is characterized by a standard deviation $\sigma = 22$ nm, which accounts for the broadening caused by carrier thermalization at 300 K.[38] The resulting profile is normalized by its peak value at $r = 0$ and fitted by a Voigt function, yielding a full width at half maximum (FWHM) of ~ 63 nm (Fig. S1**(c)**). It is important to note that our estimation does not consider the lateral carrier diffusion occurring in the surface barrier before carriers completely relax to the QW. As a result, the calculated FWHM underestimates the actual broadening of the carrier generation rate distribution in the QW. Meanwhile, the total generation rate, G_{tot} (s^{-1}), of carriers in CL can be estimated using the

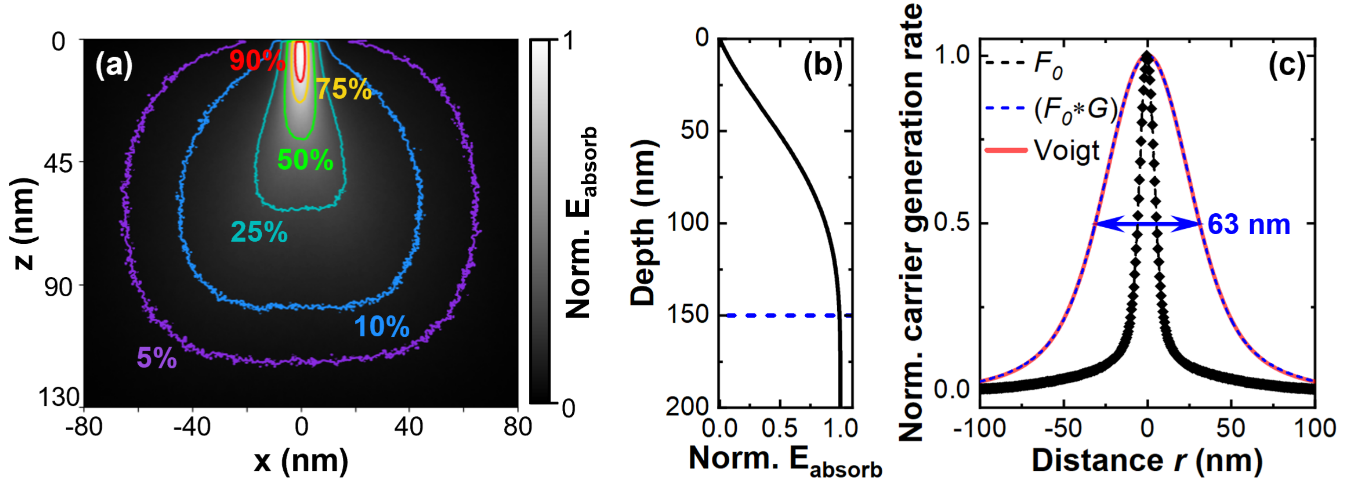

Figure S1: **(a)** Cross-section view of absorbed energy resulting from the Monte Carlo simulation of a 5 keV electron beam interacting with bulk $Al_{0.1}Ga_{0.9}N$ at 300 K. **(b)** Depth-dependent energy deposition in the sample, normalized by the total absorbed energy. **(c)** Lateral carrier generation rate distribution, $F(r)$, derived by convolving the simulated carrier generation rate distribution, $F_0(r)$, with a Gaussian function, $G(r)$, characterized by a standard deviation $\sigma = 22$ nm, accounting for the broadening due to carrier thermalization at 300 K.[38] The profile is fitted by a Voigt function with a FWHM of ~ 63 nm.

well-known equation:[39]

$$G_{\text{tot}} = \frac{I_{\text{p}}}{q} \cdot \frac{E_{\text{dep}}}{3E_{\text{g}}} , \tag{1}$$

where I_{p} is the electron beam probe current, q is the charge of an electron, E_{dep} is the average energy deposited per electron in the sample, and E_{g} is the bandgap of the sample. E_{dep} is calculated as the difference between the beam energy (E_{beam}) and the energy lost through backscattered electrons (E_{BSE}). In our case, $I_{\text{p}} = 221$ to 233 pA, measured using a Faraday cup attached to the sample holder, $E_{\text{g}} = 3.64$ eV for $Al_{0.1}Ga_{0.9}N$ at 300 K,[40] $E_{\text{beam}} = 5$ keV, and $E_{\text{BSE}} \approx 1.14$ keV computed via Monte Carlo simulation. Assuming that all generated carriers relax to the QW, the carrier generation rate in the QW, G_{QW}, is around 4.9 to $5.2 \cdot 10^{11}$ s^{-1}. Under the assumptions of carrier lifetime being independent of carrier density and no carrier diffusion in the QW, the maximal carrier density in the QW at $r = 0$ can be calculated as:

$$n_{\text{QW}}^{\text{max}} = \frac{G_{\text{QW}} \cdot \tau}{2\pi \int_0^\infty F(r) r \mathrm{d}r} , \tag{2}$$

with τ representing the carrier lifetime, which is typically around 1 ns for $GaN/Al_{0.1}Ga_{0.9}N$ structures at RT.[41,42] Hence, the estimated maximum carrier density in the QWs is approximately

8.2 to 8.7 · 10^{12} cm^{-2}. It should be noted that this value may be overestimated, considering the broader actual carrier distribution, as discussed previously. Additionally, our assumption that all carriers relax to the QW might not hold true in practice. As a result, the average carrier density in the QWs is expected to be on the order of 10^{12} cm^{-2}.

3. Optical properties of surface GaN QWs

Since the QW emission varies significantly with the surface barrier thickness, d, CL spectra of the surface GaN QWs are presented in logarithmic scale in Fig. S2(**a**), which improves the visibility of lower-intensity peaks. It is evident that, unlike surface GaAs QWs,[13] the emission intensity from our surface GaN QWs remains considerably strong even in the absence of a surface barrier. In this logscale plot, the AlGaN spacer emission from all the samples exhibits almost identical intensity. This confirms that the injection level into the samples is nearly the same, unaffected by the varying d.

For all the CL spectra analyzed in this study, a spectral deconvolution is conducted to extract detailed information of the GaN QW and AlGaN spacer emissions (Figs. S2(**b, c**)), in particular the peak energy and integrated intensity. The spectral deconvolution begins with a preliminary multi-peak fitting aimed at extracting the line shapes of the AlGaN emission and the background

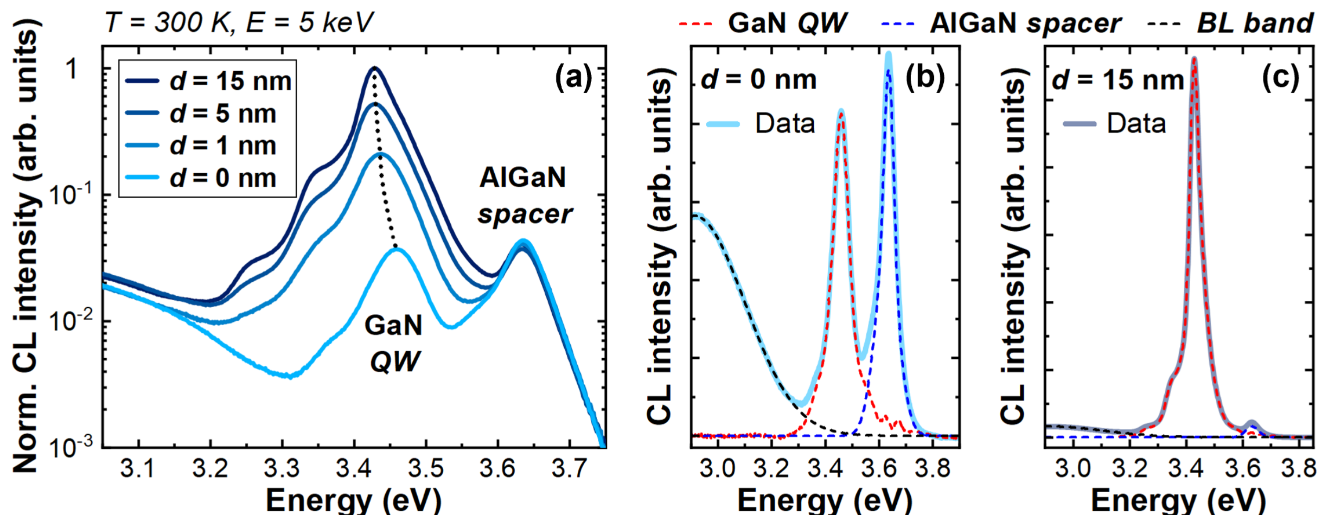

Figure S2: (**a**) CL spectra of the surface GaN QWs, excited by a 5 keV electron beam at 300 K. The intensity scale is set to logarithmic to enhance the visibility of lower-intensity peaks. (**b, c**) For each CL spectrum, a spectral deconvolution is applied to extract the peak energy and the integrated intensity of the GaN QW and AlGaN spacer emissions.

defect emission, i.e., the broad blue luminescence (BL) band peaking at ~ 2.9 eV.[43] However, for the GaN QW emission, which includes the ZPL and multiple LO phonon replicas, achieving an accurate fit is challenging. To address this, we deduced the QW emission by subtracting the fitted BL band and AlGaN emission from the raw data. This approach ensures a uniform treatment for all spectra, maintaining effective deconvolution of the overlapping QW and AlGaN emissions (Fig. S2**(b)**) while preserving the precise line shape of the entire QW emission (Fig. S2**(c)**). All the error bars in integrated intensity are estimated from the preliminary multi-peak fitting.

The peak energies of the surface GaN QWs are presented in Table 1. Notably, the peak energy of the AlGaN spacer emission remains nearly constant across all samples. In contrast, the GaN QW peak exhibits a small blueshift for the sample with $d = 1$ nm and an even larger blueshift for the uncapped QW ($d = 0$ nm). To gain insights into these observations, we conducted band diagram calculations and analyzed the corresponding confined states using the commercial software, *nextnano*,[44] as shown in Fig. S3**(a)**. For these polar surface QWs, the presence of the free surface restricts the electron wavefunction penetration into the surface barrier, which leads to enhanced quantum confinement of carriers in the well when d is small. To further analyze the emission energy as a function of d, we compared the simulated interband transition energies with the GaN QW peak energies extracted from CL measurements (Fig. S3**(b)**). While the overall d-dependent trends are in agreement, the simulated values for QWs with $d = 0, 1$ nm are much higher than the experimental data. This disparity arises from the Dirichlet boundary condition applied at the free surface in the simulation, which does not consider the evanescent wave in the vacuum, thus leading to an overestimation of the confinement energy induced by the free surface. Despite this discrepancy, the overall agreement between the two trends provides a reasonable explanation for the large blueshift observed in the uncapped QW: carrier quantum confinement in this "well" is significantly enhanced by the free surface.

Table 1: Peak energies of the GaN QW and AlGaN spacer emissions deduced from the CL spectra of surface GaN QWs with varying surface barrier thickness (d), excited by a 5 keV electron beam at 300 K.

d	**0 nm**	**1 nm**	**5 nm**	**15 nm**
GaN QW	3.459 eV	3.437 eV	3.429 eV	3.429 eV
AlGaN spacer	3.635 eV	3.635 eV	3.635 eV	3.633 eV

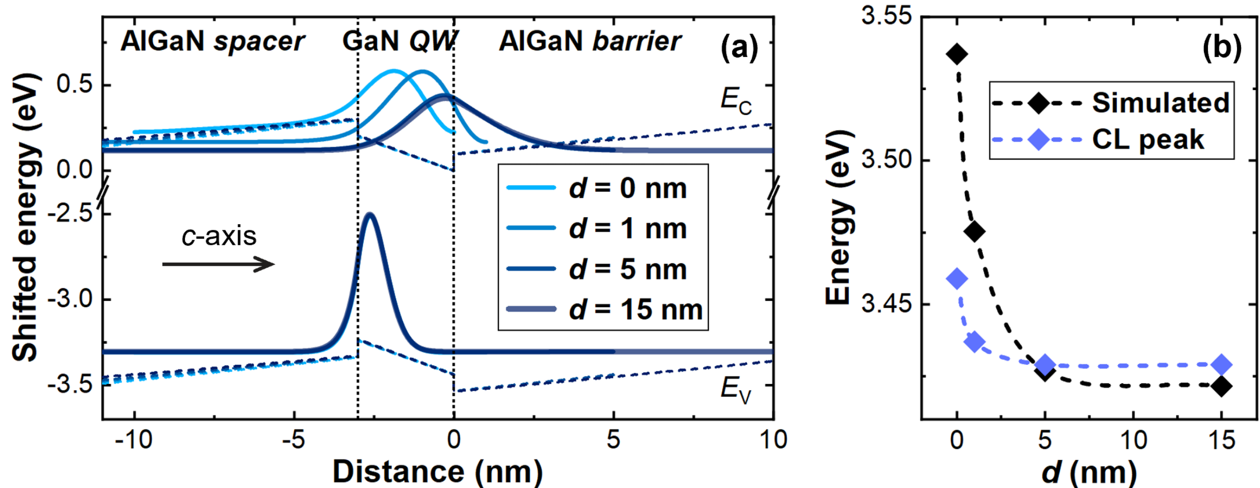

Figure S3: **(a)** Simulated band diagrams of surface GaN/AlGaN QWs with varying surface barrier thickness (d), accompanied by the corresponding wavefunction probability densities of electrons and holes in the QW region. All the wavefunction probability density curves are shifted by the energy of their associated quantized state. E_C and E_V are the conduction band minimum and valence band maximum, respectively. Based on the simulations, **(b)** the RT interband transition energy is plotted as a function of d (black diamonds), and compared to the CL data (blue diamonds).

In Fig. S4**(a)**, the integrated QW intensity is plotted against d, clearly demonstrating a nonlinear increase with increasing d. However, this is contradictory to the simulation (Fig. S3**(a)**): for larger d, the wavefunction overlap is smaller, thus the radiative recombination rate is lower. If the weight of non-radiative recombination was the same for all the samples, the QW emission intensity should decrease with increasing d. Therefore, the observed increase in intensity is dominated by a reduction in non-radiative recombination channels. Given the relation to d, these non-radiative channels are surface-related, i.e., STs.

Since the physics of the envelope function formalism fails in vacuum as there is no longer any Bloch function, we will not use the simulated wavefunctions for the comparison of the QW emission intensities. To model the d-dependent QW emission intensity, we take into account the probability of carrier tunneling from the well to the surface,[13] where carriers could potentially become trapped without emitting light, i.e., recombine non-radiatively. First of all, the measured QW emission intensity is correlated to the internal quantum efficiency of the sample, which is the ratio between the radiative recombination rate (R_r) and the effective recombination rate (R_{eff}). Given that these samples possess similar structures and were grown under identical conditions, and that their difference in confinement has a negligible impact on the emission, as previously discussed, it is reasonable to assume that R_r in these QWs remains constant. Subsequently, the QW intensity

should be inversely proportional to R_{eff}:

$$I_{\text{QW}} \propto 1/R_{\text{eff}} \,, \qquad \text{with} \quad R_{\text{eff}} = R_0 + R_{\text{NR, ST}} \,, \tag{3}$$

where R_0 represents the effective recombination rate in the absence of STs, i.e., QWs with very large d. $R_{\text{NR, ST}}$ denotes the non-radiative recombination rate associated with STs, which can be expressed as:

$$R_{\text{NR, ST}} \propto P_{\text{ST}} \cdot \int_d^{\infty} \Psi^2(x)\mathrm{d}x \,, \tag{4}$$

where P_{ST} is the probability of a surface carrier being non-radiatively trapped by STs, and Ψ is the carrier Schrödinger wavefunction, with x the distance measured along the c-axis. Here, $x = 0$ is defined at the QW-barrier interface. Hence, the integral of the probability density, Ψ^2, from d to infinity, is associated with the probability of carrier tunneling from the well to the surface. In our case, due to the presence of the built-in field, electrons in the well are more likely to cross the barrier (Fig. S3**(a)**). Therefore, they are regarded as the main carriers responsible for the tunneling from the well to the surface. Assuming a similar, albeit minor, surface band bending across all samples, the barrier height for electrons in the QWs is approximately the conduction band offset, ΔE_{C}, between the GaN QW and $Al_{0.1}Ga_{0.9}N$ barrier. This value can be estimated by considering the bandgap (E_{g}) at 300 K of GaN (3.42 eV[40]) and $Al_{0.1}Ga_{0.9}N$ (3.64 eV[40]), along with the "common anion rule":[45] $\Delta E_{\text{C}} \approx 0.7\Delta E_{\text{g}} = 154$ meV. The one-dimensional Schrödinger equation for an electron in the barrier can be written in the form:

$$\frac{d^2}{dx^2}\Psi(x) = \frac{2m^*}{\hbar^2}\Delta E_{\text{C}}\Psi(x) = \kappa^2\Psi(x) \,, \qquad \text{where} \quad \kappa^2 = \frac{2m^*}{\hbar^2}\Delta E_{\text{C}} \,. \tag{5}$$

Here $\hbar$ is the reduced Planck's constant and m^* is the effective mass of the electron in $Al_{0.1}Ga_{0.9}N$ ($m^* \approx 0.2m_0$,[46] with m_0 the electron rest mass). The solution of the equation is in the form of an evanescent wave: $\Psi(x) = \Psi_0 e^{-\kappa x}$, with Ψ_0 a constant coefficient. By inserting this expression into Eq. 4, we obtain:

$$R_{\text{NR, ST}} \propto P_{\text{ST}} \cdot e^{-2\kappa d} \,. \tag{6}$$

Given that all the samples exhibit comparable material quality, we can treat R_0 and P_{ST} as constants

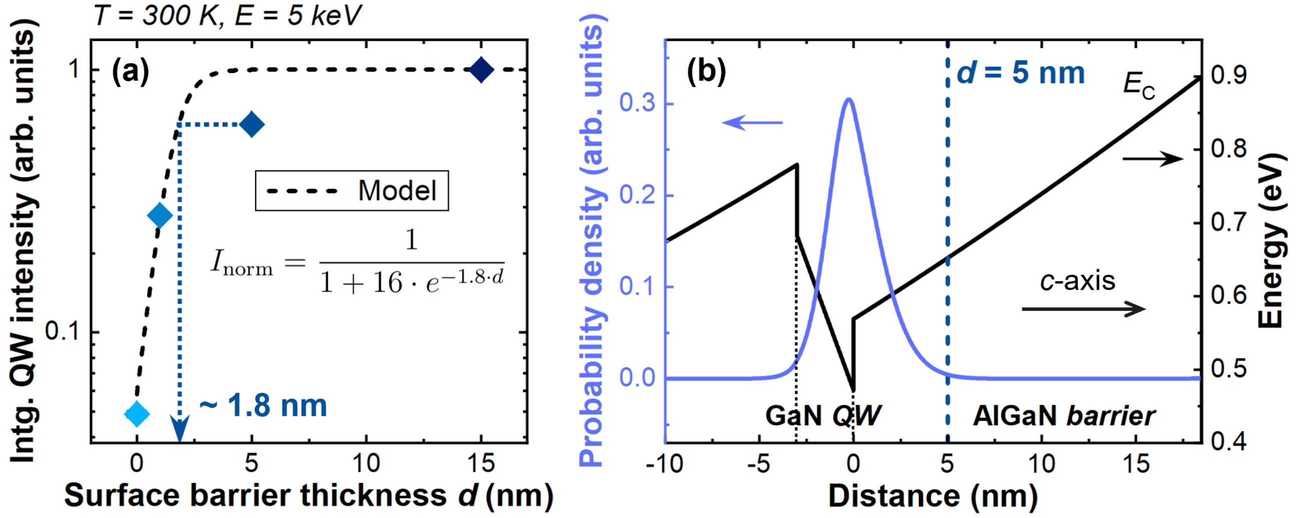

Figure S4: **(a)** d-dependent integrated QW CL intensity, excited by a 5 keV electron beam at 300 K, compared to the model, which takes into account carrier tunneling from the well to the surface. The intensity error bars are not visible in the plot as they are smaller than the size of the diamond symbol used. **(b)** Simulation of the electron wavefunction probability density across the barrier in the conduction band (E_C) imposed by a thick surface $Al_{0.1}Ga_{0.9}N$ barrier. The dark blue dashed line corresponds to the position of the free surface of the surface GaN QW with $d = 5$ nm.

independent of the variable d. Subsequently, by combining Eqs. 3 and 6, we can model the d-dependent normalized QW intensity using the following formula:

$$I_{\text{norm}}(d) = \frac{1}{1 + C \cdot e^{-2\kappa d}}\,, \qquad \text{where} \quad \lim_{d\to\infty} I_{\text{norm}} \to 1\,. \tag{7}$$

Here $\kappa \approx 0.9$, calculated using Eq. 5, and C is a parameter that can be deduced from the data. The QW CL intensity in Fig. S4**(a)** is normalized by the value at $d = 15$ nm, which aligns with the model, given that the term $e^{-2\kappa d}$ is $\sim 10^{-12}$ at $d = 15$ nm, using the previously calculated value of κ. As shown in Fig. S4**(a)**, our model (black dashed curve) successfully captures most of the experimental data, except for the point at $d = 5$ nm.

Indeed, if we compute the electron wavefunction probability density in a well with large d (Fig. S4**(b)**), the penetration is no longer affected by the boundary condition at the free surface. Electrons confined in the well have a probability of less than 1% to tunnel through a 5 nm $Al_{0.1}Ga_{0.9}N$ barrier (indicated by the dark blue dashed line). The observed increase in intensity when d increases from 5 nm to 15 nm suggests that the effective thickness (d_{eff}) of the 5 nm thick AlGaN barrier, acting as an "electron blocking layer", is significantly smaller than its physical size. In fact, for the same intensity in the model's curve, the corresponding barrier thickness is ~ 1.8 nm

(indicated by the dark blue dotted arrow in Fig. S4(**a**)), i.e., ~ 3.2 nm less than the actual thickness. A possible explanation for this discrepancy is the presence of percolative paths in the AlGaN barrier caused by alloy disorder.[47] The random distribution of Al atoms in the barrier results in regions of varying Al content, known as alloy disorder. In other words, if we consider the same Al content in the barrier, it implies that d_{eff} is locally changing. Since $d = 5$ nm is at the limit of carrier tunneling (Fig. S4(**b**)), for regions where $d_{\text{eff}} > 5$ nm, there is no significant impact on the emission. However, in regions where $d_{\text{eff}} < 5$ nm, the intensity can be dramatically affected. Thus, the overall consequence of the percolative paths within the 5 nm thick AlGaN barrier is a reduction in d_{eff}. Considering the typical scale of alloy disorder in the III-nitride system, i.e., the average size of the Al-free regions in our case, is ~ 3 nm,[48] the disorder-induced percolation effect is consistent with the observed difference between the physical and effective thickness for $d = 5$ nm. Regarding the other two samples with smaller d, fluctuations in both directions (decreasing and increasing d) lead to changes in the intensity. Therefore, the order of magnitude of the intensity for these samples is less affected by the percolation effect. As a result, unlike the sample with $d = 5$ nm, the values of these samples align well with the model, as shown in Fig. S4(**a**).

To summarize the findings discussed so far, we model the d-dependent QW intensity by considering the carrier tunneling effect, and deduce that the presence of alloy disorder in the AlGaN barrier reduces its effective thickness. This leads to surface-sensitive QW emission even with a relatively thick barrier. Among all the samples studied, only the QW with $d = 15$ nm appears to be entirely unaffected by surface effects. To further understand the impact of alloy disorder in the barrier, additional investigations, such as transmission electron microscopy, and comparison with QWs using GaN barriers, which lack alloy disorder, are necessary. These investigations are currently in progress in our group.

In order to investigate the change in the QW emission line shape under different injection levels, we compare the CL spectra with the PL spectra of the same samples. The PL spectra were obtained using a cw laser with a power density of ~ 16 W/cm^2 at a wavelength of 325 nm. Under this excitation condition, assuming that nearly all carriers relax to the QW and using the previously employed carrier lifetime of 1 ns, the estimated carrier density in the QWs is on the order of 10^{10} cm^{-2} in PL,[49] which is nearly two orders of magnitude lower than the estimated carrier density in CL (SI Sec. 2). As depicted in Fig. S5, the CL peaks are generally blueshifted by ~ 30 meV, which can

be attributed to a stronger screening of the built-in field in the QW caused by the higher carrier density. On the other hand, the line shape of the QW peaks remains nearly identical between CL and PL spectra. If the carrier density in CL were above the critical density of the Mott transition, a much more asymmetric line shape would be expected due to band filling of the continuum states.[26] Our observation strongly suggests that in the CL measurements, carriers in the QWs predominantly exist as excitons rather than unbound electron-hole pairs. Consequently, the emission studied in this work is primarily governed by excitonic features.

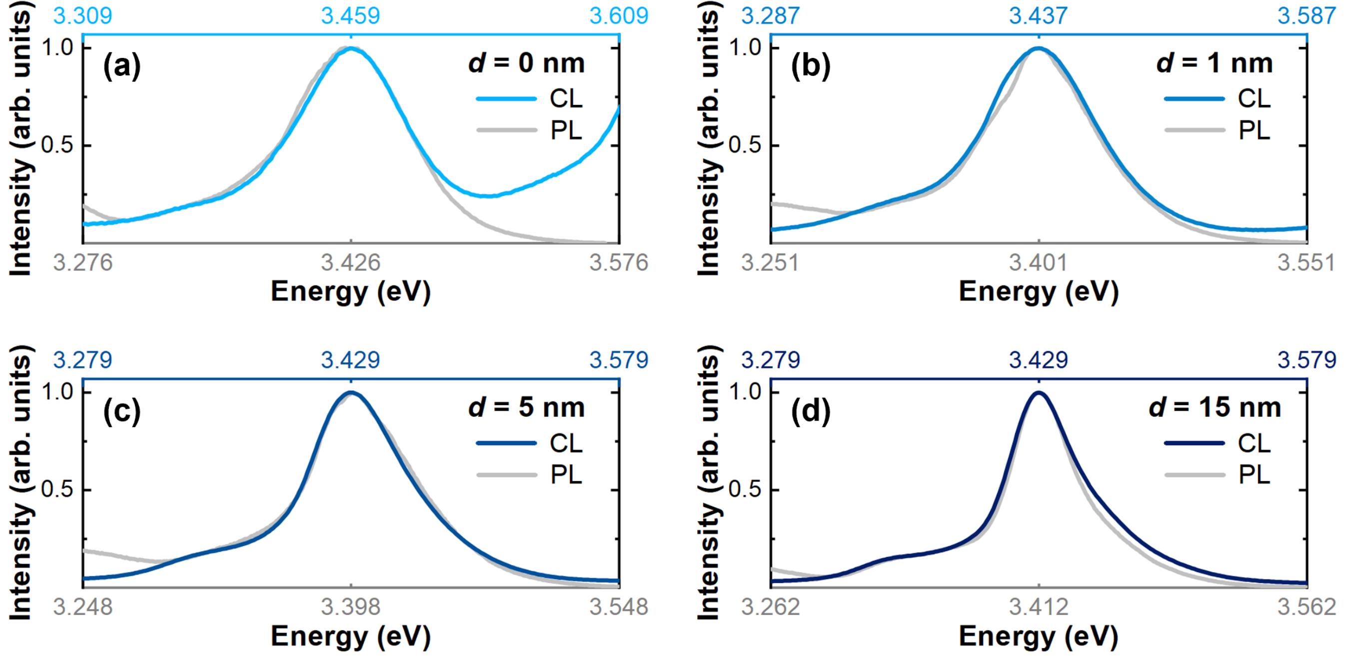

Figure S5: Comparison of the QW emission line shape under different injection conditions: lower carrier density ($\sim 10^{10}$ cm^{-2}) in PL and higher carrier density ($\sim 10^{12}$ cm^{-2}) in CL at 300 K, for surface GaN QWs with varying barrier thickness: **(a)** $d = 0$ nm, **(b)** $d = 1$ nm, **(c)** $d = 5$ nm, and **(d)** $d = 15$ nm. The energy axis of the CL spectra is shifted to match the peak energy in the PL spectra while maintaining the same scale.

4. Thickness determination of MoS_2

2D MoS_2 flakes were first obtained by mechanically exfoliating bulk MoS_2 crystals, and deposited onto a Si substrate pre-coated with a 275 nm thick SiO_2 layer. This particular thickness of oxide was chosen to optimize the visibility of ML-MoS_2 under the optical microscope, based on light interference.[50] The flakes of interest were initially identified using optical microscopy (Fig. S6**(a)**), and their thickness was subsequently determined by AFM (Fig. S6**(b)**). For our MoS_2 samples

with lateral thickness variation, we estimated the layer thickness in different regions based on the typical ML-MoS_2 thickness of $\sim$ 0.65 nm. However, it must be acknowledged that in the AFM measurements, ML-flakes on bare substrates showed a broad distribution in heights, ranging from 0.6 to 0.9 nm,[51] which may be due to the presence of adsorbates beneath the flake or other flake-substrate interactions.[52]

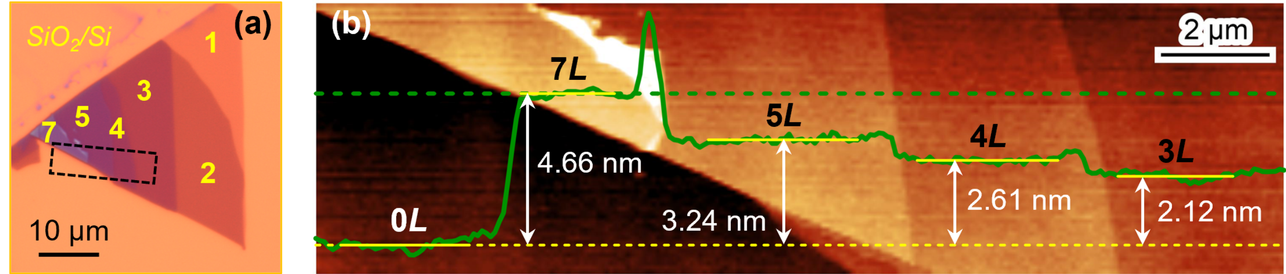

Figure S6: **(a)** Optical micrograph of the selected MoS_2 flake, deposited on a SiO_2/Si substrate. The numbers in yellow indicate the number of MoS_2 MLs in the corresponding region, determined by AFM and Raman spectroscopy. **(b)** AFM height image of the rectangular area outlined by the black dashed line in **(a)**. The thickness of each layer is determined from the height profile (green solid curve) taken along the green dashed line in the AFM image. The "nL" labels indicate that the MoS_2 thickness in the corresponding region is n MLs.

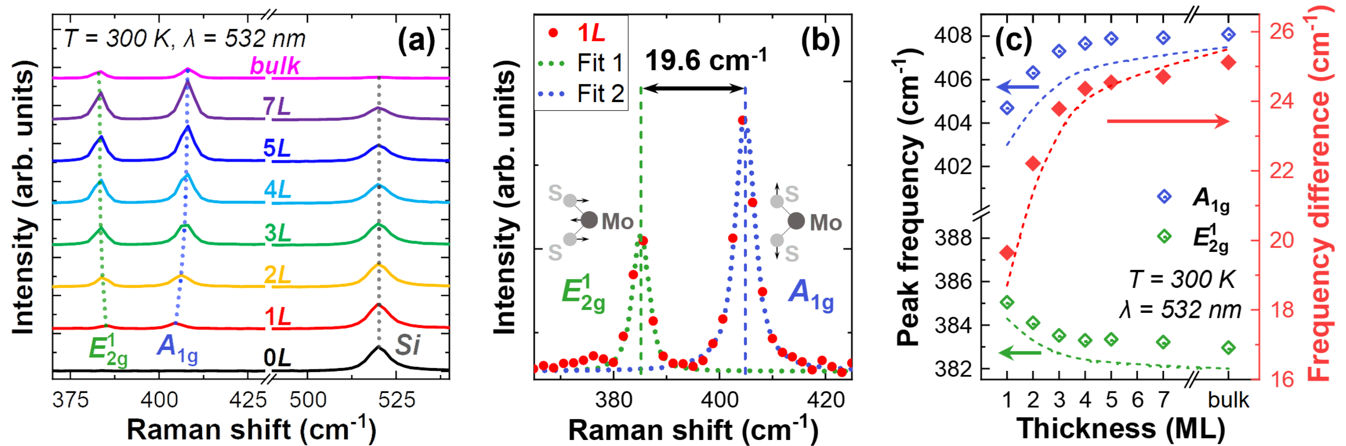

Figure S7: **(a)** Raman spectra obtained from various regions of the MoS_2 flake as illustrated in Fig. S6**(a)**. Each spectrum is labelled with the layer thickness (number of MLs, nL) estimated through AFM measurements. A double-Voigt fit is applied to each spectrum to extract the peak frequencies of the E^1_{2g} and A_{1g} Raman modes. **(b)** In the ML-MoS_2 region (1L), the difference between the two peaks is $\sim$ 19.6 cm^{-1}, which falls within the expected range of ML-MoS_2. **(c)** The frequencies of the E^1_{2g} and A_{1g} Raman modes (left vertical axis) and their difference (right vertical axis) are plotted as a function of layer thickness. Our results (diamonds) are compared with the expected trends (dashed curves).[51]

To double-check the layer thickness, Raman spectroscopy measurements were carried out in different regions using a cw 532 nm laser in an air ambient environment (Fig. S7**(a)**). This method

is based on the fact that the Raman frequencies of the E^1_{2g} mode (in-plane opposite vibrations of S and Mo atoms, illustrated in Fig. S7(**b**)) and the A_{1g} mode (out-of-plane vibration of S atoms in opposite directions, illustrated in Fig. S7(**b**)) are highly sensitive to MoS_2 thickness within the range of 1-4 MLs.[51] Especially, the difference between the two peaks in ML-MoS_2 generally falls within the range of 18-21 cm^{-1}, regardless of the laser[53] or substrate[54] used. Therefore, this feature is commonly used to identify ML-MoS_2. In our case, the observed thickness-dependent Raman peaks and the frequency difference between the two peaks (diamonds in Fig. S7(**c**)) align well with the reported trend (dashed curves in Fig. S7(**c**)),[51] thus corroborating the thickness determined by AFM. Furthermore, the presence of a ML-MoS_2 region ($1L$) in the flakes of interest, which is crucial for our study, is well confirmed (Fig. S7(**b**)).

5. CL data processing

The hyperspectral analysis was conducted using the *hyperspy* package in Python.[55] For each pixel in the hyperspectral map, a multi-peak fitting is employed to extract the integrated intensity of the GaN QW and AlGaN spacer emissions (Figs. S8(**a, b**)), which enables the generation of integrated intensity maps for each emission within the scanned area (Figs. S8(**c, d**)).

To extract information from regions with different MoS_2 thicknesses, we employed image segmentation on the high-resolution optical micrograph of the flake (Figs. S9(**a, b**)). This is based on the thickness-sensitive color contrast mentioned earlier. Consequently, regions with different

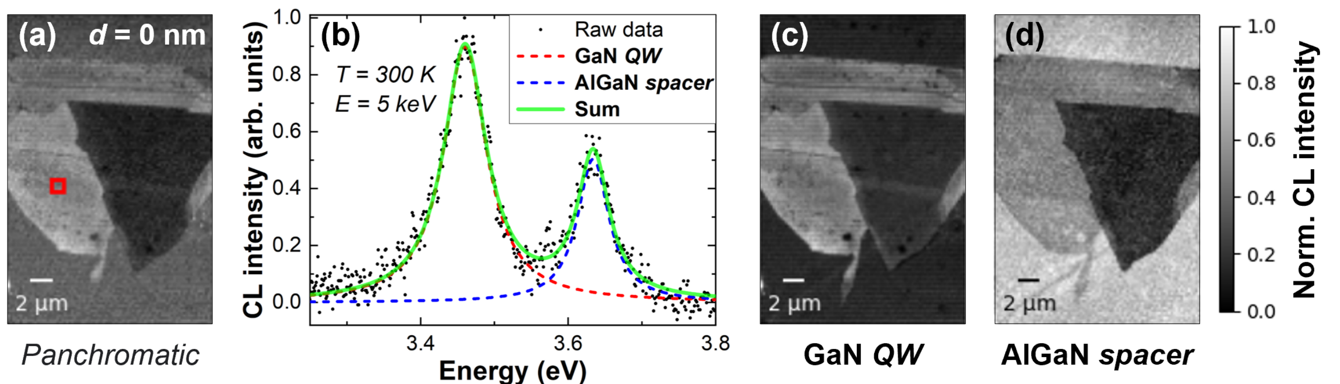

Figure S8: (**a**) Panchromatic CL map of the uncapped QW ($d = 0$ nm) coated with MoS_2, measured at 300 K using a 5 keV electron beam. (**b**) Normalized RT CL spectrum acquired at the pixel represented by the red square in (**a**). By performing multi-peak fitting for all pixels, integrated intensity maps of the (**c**) GaN QW and (**d**) AlGaN spacer emissions are generated. All maps are individually normalized by their maximum and minimum values.

thicknesses are assigned specific colors, i.e., defined pixel values. The resulting segmented image was then rotated and resized to align it with the contour of the flake in the panchromatic CL map (Fig. S9(**c**)). The reshaped image was subsequently cropped and binned to generate a mask for the CL map, ensuring that its image size and number of pixels are the same as the CL map (Fig. S9(**d**)). Due to the lower resolution of the CL map, pixels located at the boundaries of the segmented regions exhibit intermediate values after the binning process. To address this, all these new pixel values were converted to (255, 255, 255) (white in color), which represent "dead pixels" and are excluded from further data processing and analysis. For all the CL maps in this study, we generated an associated mask where the color of each pixel represents the number of MoS_2 MLs at that position.

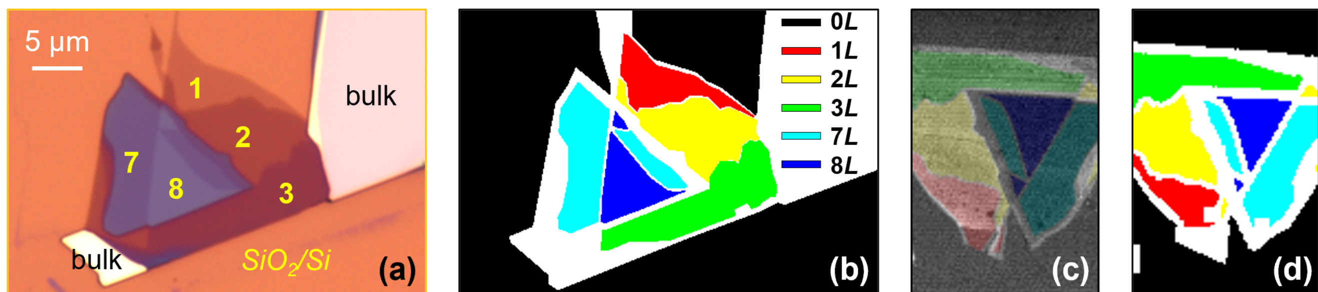

Figure S9: **(a)** High-resolution optical micrograph of the MoS_2 flake deposited on a SiO_2/Si substrate, which is **(b)** segmented according to thickness-sensitive color contrast. **(c)** The segmented image is rotated and resized to match the flake in the CL map. **(d)** After cropping, pixel binning, and dead pixel identification, a mask of the CL map is generated

The use of thickness-related masks is crucial to our study. Firstly, these masks enable the calculation of the average background intensity (I_{Bkg}) in different emission maps, which allows equivalent normalization of the maps and facilitates comparison across different samples. Specifically, the normalized intensity is calculated using $I_{\mathrm{norm}} = I/I_{\mathrm{Bkg}}$, so that the average background intensity is set to 1 for all maps. In this way, the contrast observed in each map represents the relative change in intensity induced by the presence of MoS_2, allowing direct comparisons between different maps. Secondly, instead of comparing solely the intensity maps that primarily reflect spatial variations related to the surface morphology of the sample, we also focus on the spectral domain by comparing the average spectra obtained from regions coated with MoS_2 of different thicknesses. The advantage of this analysis is twofold. On the one hand, the average spectrum captures the general properties of the interface effect associated with MoS_2 thickness and effectively minimizes

the impact of microscale fluctuations arising from surface roughness or other factors that are not the main focus of this study. On the other hand, by averaging a large number of spectra, the resulting spectrum has a higher signal-to-noise ratio. This facilitates quantitative analyses, including the peak identification (e.g., ZPL and LO phonon replicas of the GaN QW emission) and the calculation of energy-dependent intensity contrasts (see Fig. 5(**b**) in the main text). Overall, the use of thickness-related masks enables equivalent data normalization, spectral analysis, and quantitative calculations, which improves the interpretability and reliability of our results.

6. MoS_2 on bulk GaN epilayer

To confirm the hypothesis of the surface passivation effect, we deposited an MoS_2 flake of 1-3 MLs on a bulk GaN epilayer, identical to the GaN buffer used to grow the QWs (SI Sec. 1). CL measurement was performed on this flake at 300 K using 5 keV excitation. The resulting GaN intensity map is normalized (inset of Fig. S10(**a**)) and compared to the normalized GaN QW intensity map of the uncapped GaN QW ($d = 0$ nm) coated with 2D MoS_2 (inset of Fig. S10(**b**)). Through normalization, both maps have the same average background intensity, i.e., 1. Upon comparison, it is evident that both maps demonstrate enhanced GaN emission in the presence of MoS_2. However, the enhancement is obviously stronger for the uncapped GaN QW emission than

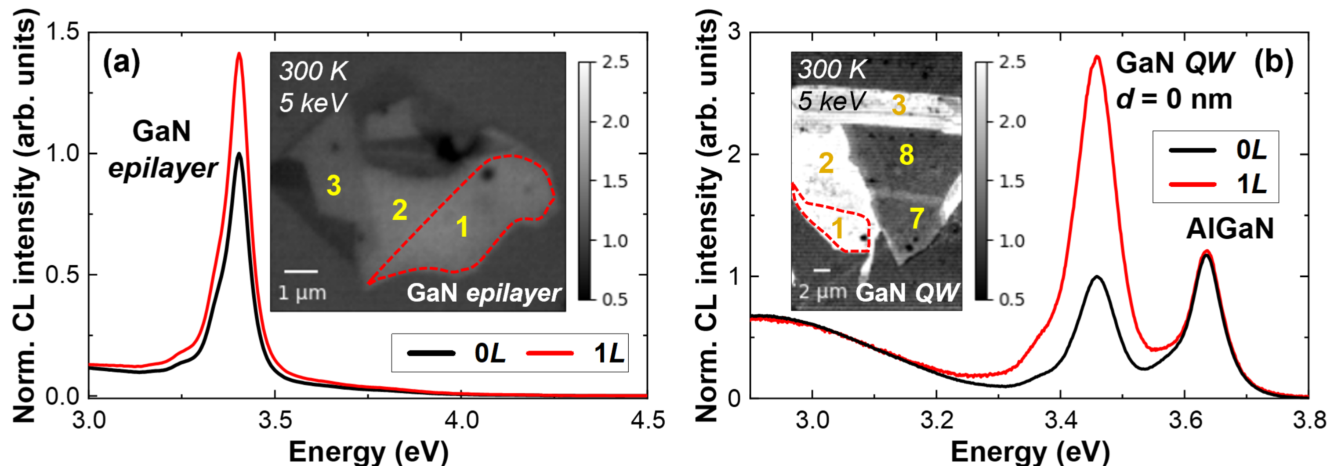

Figure S10: Average RT CL spectra of the background emission (in absence of MoS_2, $0L$) and the emission from the region covered by ML-MoS_2 ($1L$) extracted from (**a**) the GaN epilayer and (**b**) the uncapped GaN QW ($d = 0$ nm), both coated with a MoS_2 flake. The corresponding integrated GaN CL intensity maps are shown in the insets, with the $1L$ region indicated by the red dashed line. These maps are normalized by their average background intensity, respectively.

for the GaN epilayer emission. To quantitatively visualize this difference, average CL spectra of the bare region ($0L$) and the region coated with ML-MoS_2 ($1L$) are compared. For the GaN epilayer, the emission is enhanced by ML-MoS_2, with a peak intensity ratio of ~ 1.4 (Fig. S10(**a**)). In contrast, for the uncapped QW, only the GaN QW emission is enhanced, but with a higher peak intensity ratio of ~ 2.8 (Fig. S10(**b**)). This discrepancy in MoS_2-induced intensity enhancement between the two cases is consistent with the surface passivation effect. In the uncapped QW, the detected GaN emission comes solely from the surface region, whereas in the GaN epilayer, the emission arises from both surface and bulk regions. As a result, the enhancement is much greater in the former case due to the direct influence of surface passivation.

7. MoS_2 on GaN QW, $d = 15$ nm

The presence of ML-MoS_2 enhances the AlGaN emission from the GaN QW with $d = 15$ nm (see Fig. 5(**b**) in the main text). This enhancement can be attributed to the surface passivation induced by the deposition of ML-MoS_2, as illustrated in Fig. S11. In the case of a bare QW without the deposition of MoS_2 (Fig. S11(**a**)), potential emission in the AlGaN surface barrier is quenched due to the presence of STs. Consequently, the AlGaN emission primarily originates from the spacer region, situated far from the surface. Upon the deposition of ML-MoS_2 (Fig. S11(**b**)), the change in surface band bending[12] results in the filling of STs by charges transferred through the vdW

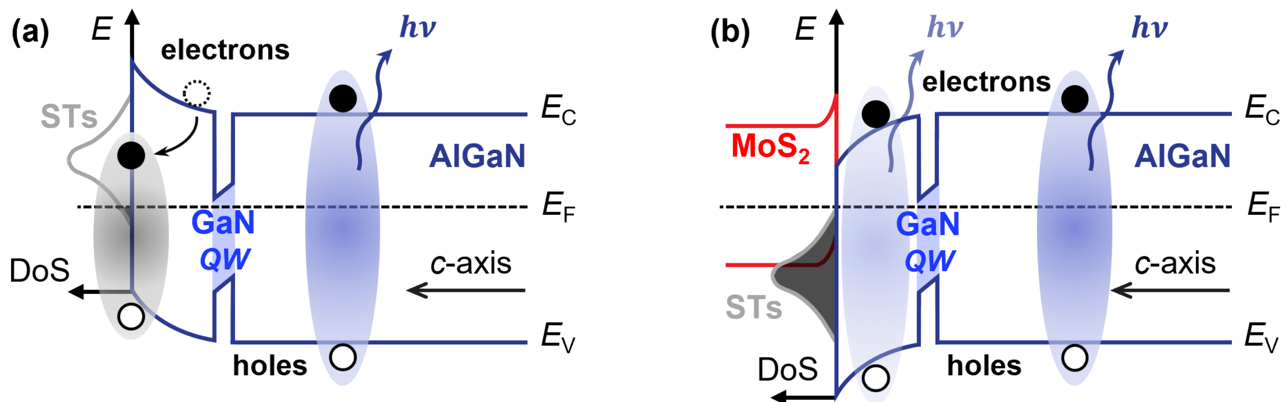

Figure S11: Surface band bending of (**a**) bare GaN QW with $d = 15$ nm and (**b**) the QW coated with MoS_2 following interfacial charge transfer.[12] The density of states (DoS) of surface traps (STs) in the AlGaN surface barrier is depicted for both scenarios, with the black shaded part representing occupied states. The grey ellipse represents an exciton captured by a ST and does not emit light, while the blue ellipses represent free excitons that can emit light through radiative recombination.

interface. As the occupied STs are no longer capable of capturing excitons in the surface region, the emission from the surface AlGaN barrier could potentially be enhanced, which results in an overall increase in the AlGaN emission in the presence of ML-MoS_2 coating.

8. MoS_2 on GaN QWs, $d = 1$ nm and $d = 5$ nm

Detailed CL results of the QW with $d = 5$ nm are presented in Fig. S12. This includes the optical micrograph of the MoS_2 flake deposited on a SiO_2/Si substrate (Fig. S12(**a**)), the integrated QW CL intensity map (Fig. S12(**b**)), and the average CL spectra extracted from the hyperspectral map using the segmentation mask (Fig. S12(**c**)).

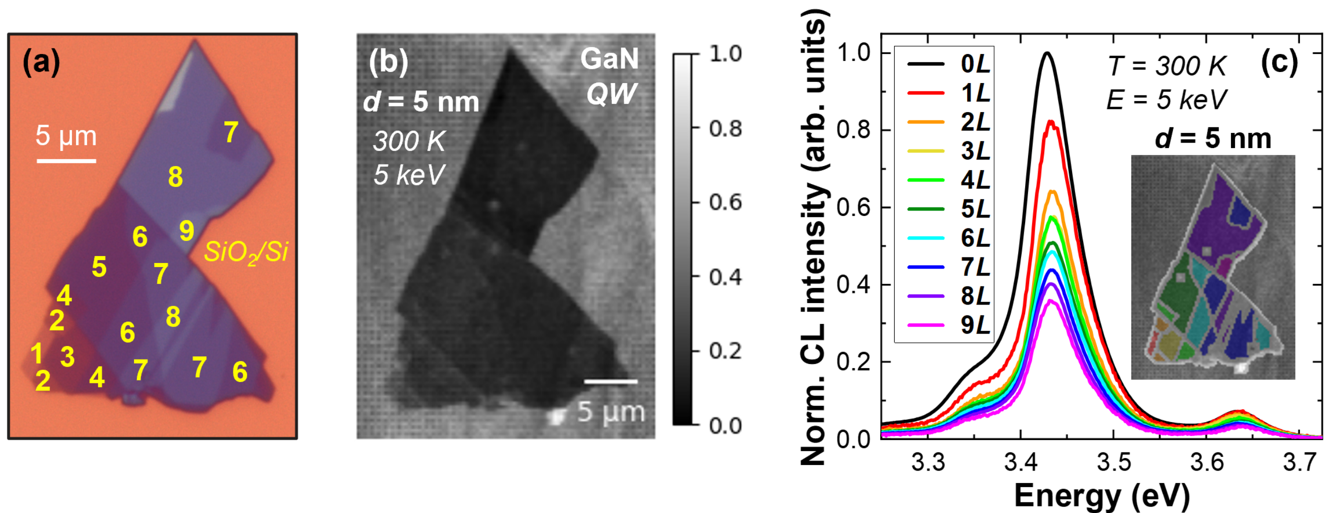

Figure S12: (**a**) Optical micrograph of the MoS_2 flake on a SiO_2/Si substrate. The yellow numbers indicate the number of MoS_2 MLs in the corresponding region. (**b**) Normalized integrated CL intensity map of the GaN QW emission obtained from the MoS_2-coated QW with $d = 5$ nm, excited by a 5 keV electron beam at 300 K. The normalization is done with respect to the maximum and minimum values in the map. (**c**) Average RT CL spectra extracted from regions with different MoS_2 thicknesses. The corresponding regions are shown in the inset.

By extracting average spectra from regions with varying MoS_2 thicknesses across all the samples in the series, we calculated the CL intensity contrast between the background ($0L$) and the region coated with ML-MoS_2 ($1L$), as well as between two other regions with MoS_2 thickness differing by 1 ML (nL and $(n+1)L$, with $n > 0$). As shown in Fig. S13, the contrast observed in other regions, induced by the presence of the additional ML-MoS_2 ($(n+1)L$-to-nL, light blue curve) aligns with ML-MoS_2 spectral absorptance[23] (black dashed curve). However, the contrast observed on the QW surface, resulting from the deposition of a single ML-MoS_2 ($1L$-to-$0L$, blue curve),

differs significantly from the absorption behavior and displays distinct peaks associated with the QW emissions. It is worth noting that the shape of these contrast peaks varies between different samples, which is likely due to variations in excitonic transitions within the QWs of different d, influenced by structural or material disorders that arise during the growth process. Let us focus on the peak around 3.4 eV (indicated by the red arrow), which corresponds to the ZPL of the QWs. The peak contrast is $\sim 36\%$ for $d = 15$ nm (Fig. S13(**a**)), $\sim 42\%$ for $d = 5$ nm (Fig. S13(**b**)), and $\sim 52\%$ for $d = 1$ nm (Fig. S13(**c**)). The amplitude of this peak reflects the strength of the excitonic interactions between the GaN QW and ML-MoS_2. It is evident that the interaction strength is strongly dependent on the distance between the two materials, i.e., d. This observation is in line with the mechanism of FRET.[17]

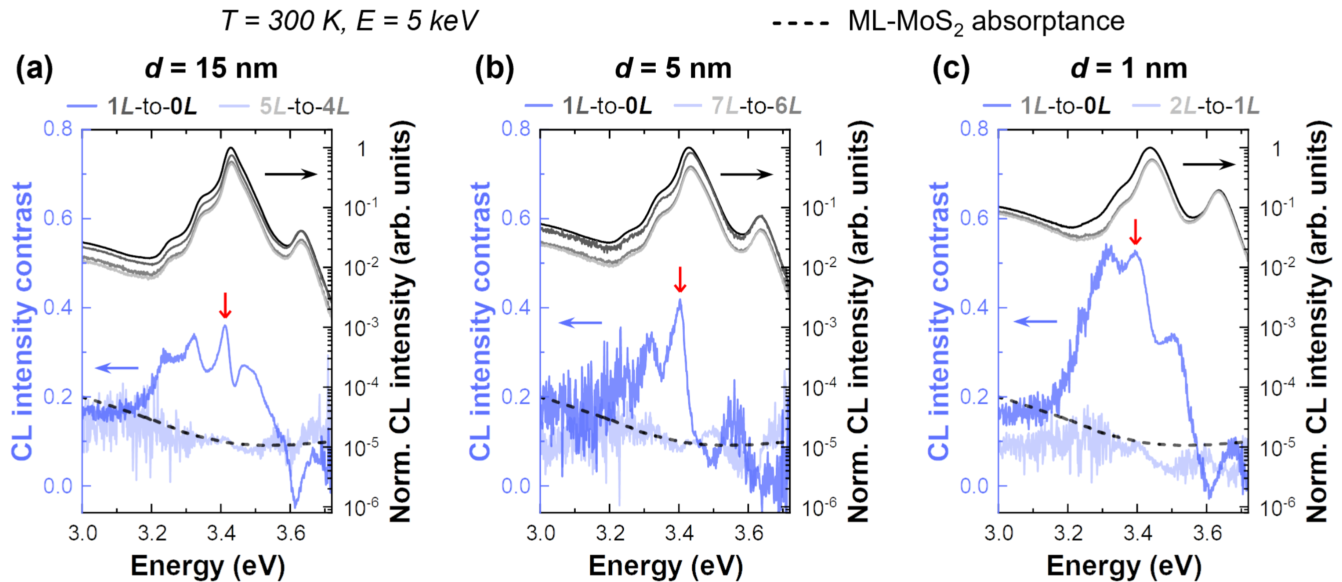

Figure S13: The blue curves represent the CL intensity contrast between the background region ($0L$) and the region coated with ML-MoS_2 ($1L$). The light blue curves represent the CL intensity contrast between regions coated with n and $(n+1)$ MLs of MoS_2, where $n > 0$. The black dashed curves represent the reported spectral absorptance of ML-MoS_2.[23] The data is obtained from surface GaN QWs with (**a**) $d = 15$ nm, (**b**) $d = 5$ nm, and (**c**) $d = 1$ nm. The related CL spectra are plotted to illustrate the energy range of different emissions. The colors of the spectra correspond to the colors used for their labels, nL, representing the number of MoS_2 MLs in the corresponding region.

References

(1) Nakamura, S.; Mukai, T.; Senoh, M. Candela-class high-brightness InGaN/AlGaN double-heterostructure blue-light-emitting diodes. *Appl. Phys. Lett.* **1994**, *64*, 1687–1689.

(2) Steube, M.; Reimann, K.; Fröhlich, D.; Clarke, S. J. Free excitons with $n = 2$ in bulk GaN. *Appl. Phys. Lett.* **1997**, *71*, 948–949.

(3) Malpuech, G.; Di Carlo, A.; Kavokin, A.; Baumberg, J. J.; Zamfirescu, M.; Lugli, P. Room-temperature polariton lasers based on GaN microcavities. *Appl. Phys. Lett.* **2002**, *81*, 412–414.

(4) Christopoulos, S.; von Högersthal, G. B. H.; Grundy, A. J. D.; Lagoudakis, P. G.; Kavokin, A. V.; Baumberg, J. J.; Christmann, G.; Butté, R.; Feltin, E.; Carlin, J.-F.; Grandjean, N. Room-temperature polariton lasing in semiconductor microcavities. *Phys. Rev. Lett.* **2007**, *98*, 126405.

(5) Novoselov, K. S.; Geim, A. K.; Morozov, S. V.; Jiang, D.; Zhang, Y.; Dubonos, S. V.; Grigorieva, I. V.; Firsov, A. A. Electric field effect in atomically thin carbon films. *Science* **2004**, *306*, 666–669.

(6) Chaves, A. et al. Bandgap engineering of two-dimensional semiconductor materials. *npj 2D Mater. Appl.* **2020**, *4*, 29.

(7) Britnell, L.; Ribeiro, R. M.; Eckmann, A.; Jalil, R.; Belle, B. D.; Mishchenko, A.; Kim, Y.-J.; Gorbachev, R. V.; Georgiou, T.; Morozov, S. V.; Grigorenko, A. N.; Geim, A. K.; Casiraghi, C.; Neto, A. H. C.; Novoselov, K. S. Strong light-matter interactions in heterostructures of atomically thin films. *Science* **2013**, *340*, 1311–1314.

(8) Mueller, T.; Malic, E. Exciton physics and device application of two-dimensional transition metal dichalcogenide semiconductors. *npj 2D Mater. Appl.* **2018**, *2*, 29.

(9) Ciarrocchi, A.; Tagarelli, F.; Avsar, A.; Kis, A. Excitonic devices with van der Waals heterostructures: valleytronics meets twistronics. *Nat. Rev. Mater.* **2022**, *7*, 449–464.

(10) Li, D.; Cheng, R.; Zhou, H.; Wang, C.; Yin, A.; Chen, Y.; Weiss, N. O.; Huang, Y.; Duan, X.

Electric-field-induced strong enhancement of electroluminescence in multilayer molybdenum disulfide. *Nat. Commun.* **2015**, *6*, 7509.

(11) Zhang, Z.; Qian, Q.; Li, B.; Chen, K. J. Interface engineering of monolayer MoS_2/GaN hybrid heterostructure: modified band alignment for photocatalytic water splitting application by nitridation treatment. *ACS Appl. Mater. Interfaces* **2018**, *10*, 17419–17426.

(12) Jain, S. K.; Kumar, R. R.; Aggarwal, N.; Vashishtha, P.; Goswami, L.; Kuriakose, S.; Pandey, A.; Bhaskaran, M.; Walia, S.; Gupta, G. Current transport and band alignment study of MoS_2/GaN and MoS_2/AlGaN heterointerfaces for broadband photodetection application. *ACS Appl. Electron. Mater.* **2020**, *2*, 710–718.

(13) Chang, Y.-L.; Tan, I.-H.; Zhang, Y.-H.; Bimberg, D.; Merz, J.; Hu, E. Reduced quantum efficiency of a near-surface quantum well. *J. Appl. Phys.* **1993**, *74*, 5144–5148.

(14) Bulashevich, K. A.; Karpov, S. Y. Impact of surface recombination on efficiency of III-nitride light-emitting diodes. *Phys. Status Solidi RRL* **2016**, *10*, 480–484.

(15) Grandjean, N.; Damilano, B.; Dalmasso, S.; Leroux, M.; Laügt, M.; Massies, J. Built-in electric-field effects in wurtzite AlGaN/GaN quantum wells. *J. Appl. Phys.* **1999**, *86*, 3714–3720.

(16) Bernardini, F.; Fiorentini, V.; Vanderbilt, D. Spontaneous polarization and piezoelectric constants of III-V nitrides. *Phys. Rev. B* **1997**, *56*, R10024–R10027.

(17) Förster, T. Transfer mechanisms of electronic excitation energy. *Radiat. Res. Suppl.* **1960**, *2*, 326–339.

(18) Achermann, M.; Petruska, M. A.; Kos, S.; Smith, D. L.; Koleske, D. D.; Klimov, V. I. Energy-transfer pumping of semiconductor nanocrystals using an epitaxial quantum well. *Nature* **2004**, *429*, 642–646.

(19) Gonzalez, J. C.; Bunker, K. L.; Russell, P. E. Minority-carrier diffusion length in a GaN-based light-emitting diode. *Appl. Phys. Lett.* **2001**, *79*, 1567–1569.

(20) Van de Walle, C. G.; Segev, D. Microscopic origins of surface states on nitride surfaces. *J. Appl. Phys.* **2007**, *101*, 081704.

(21) Seong, T.-Y.; Amano, H. Surface passivation of light emitting diodes: From nano-size to conventional mesa-etched devices. *Surf. Interfaces* **2020**, *21*, 100765.

(22) Li, H.; Wu, J.; Huang, X.; Lu, G.; Yang, J.; Lu, X.; Xiong, Q.; Zhang, H. Rapid and reliable thickness identification of two-dimensional nanosheets using optical microscopy. *ACS Nano* **2013**, *7*, 10344–10353.

(23) Dumcenco, D.; Ovchinnikov, D.; Marinov, K.; Lazić, P.; Gibertini, M.; Marzari, N.; Sanchez, O. L.; Kung, Y.-C.; Krasnozhon, D.; Chen, M.-W.; Bertolazzi, S.; Gillet, P.; Fontcuberta i Morral, A.; Radenovic, A.; Kis, A. Large-area epitaxial monolayer MoS_2. *ACS Nano* **2015**, *9*, 4611–4620.

(24) Castellanos-Gomez, A.; Quereda, J.; van der Meulen, H. P.; Agraït, N.; Rubio-Bollinger, G. Spatially resolved optical absorption spectroscopy of single- and few-layer MoS_2 by hyperspectral imaging. *Nanotechnology* **2016**, *27*, 115705.

(25) Negri, M.; Francaviglia, L.; Dumcenco, D.; Bosi, M.; Kaplan, D.; Swaminathan, V.; Salviati, G.; Kis, A.; Fabbri, F.; Fontcuberta i Morral, A. Quantitative nanoscale absorption mapping: a novel technique to probe optical absorption of two-dimensional materials. *Nano Lett.* **2020**, *20*, 567–576.

(26) Rossbach, G.; Levrat, J.; Jacopin, G.; Shahmohammadi, M.; Carlin, J.-F.; Ganière, J.-D.; Butté, R.; Deveaud, B.; Grandjean, N. High-temperature Mott transition in wide-band-gap semiconductor quantum wells. *Phys. Rev. B* **2014**, *90*, 201308.

(27) Shahmohammadi, M.; Jacopin, G.; Rossbach, G.; Levrat, J.; Feltin, E.; Carlin, J.-F.; Ganière, J.-D.; Butté, R.; Grandjean, N.; Deveaud, B. Biexcitonic molecules survive excitons at the Mott transition. *Nat. Commun.* **2014**, *5*, 5251.

(28) Klingshirn, C. F. *Semiconductor optics*; Springer: Berlin; New York, 2005.

(29) Hofstetter, D.; Beck, H.; Epler, J. E.; Kirste, L.; Bour, D. P. Evidence of strong electron-phonon interaction in a GaN-based quantum cascade emitter. *Superlattices Microstruct.* **2020**, *145*, 106631.

(30) Itskos, G.; Heliotis, G.; Lagoudakis, P. G.; Lupton, J.; Barradas, N. P.; Alves, E.; Pereira, S.; Watson, I. M.; Dawson, M. D.; Feldmann, J.; Murray, R.; Bradley, D. D. C. Efficient dipole-dipole coupling of Mott-Wannier and Frenkel excitons in (Ga,In)N quantum well/polyfluorene semiconductor heterostructures. *Phys. Rev. B* **2007**, *76*, 035344.

(31) Prins, F.; Goodman, A. J.; Tisdale, W. A. Reduced dielectric screening and enhanced energy transfer in single- and few-layer MoS_2. *Nano Lett.* **2014**, *14*, 6087–6091.

(32) Taghipour, N.; Hernandez Martinez, P. L.; Ozden, A.; Olutas, M.; Dede, D.; Gungor, K.; Erdem, O.; Perkgoz, N. K.; Demir, H. V. Near-unity efficiency energy transfer from colloidal semiconductor quantum wells of CdSe/CdS nanoplatelets to a monolayer of MoS_2. *ACS Nano* **2018**, *12*, 8547–8554.

(33) Feltin, E.; Simeonov, D.; Carlin, J.-F.; Butté, R.; Grandjean, N. Narrow UV emission from homogeneous GaN/AlGaN quantum wells. *Appl. Phys. Lett.* **2007**, *90*, 021905.

(34) Wang, L.; Meric, I.; Huang, P. Y.; Gao, Q.; Gao, Y.; Tran, H.; Taniguchi, T.; Watanabe, K.; Campos, L. M.; Muller, D. A.; Guo, J.; Kim, P.; Hone, J.; Shepard, K. L.; Dean, C. R. One-dimensional electrical contact to a two-dimensional material. *Science* **2013**, *342*, 614–617.

(35) Castellanos-Gomez, A.; Duan, X.; Fei, Z.; Gutierrez, H. R.; Huang, Y.; Huang, X.; Quereda, J.; Qian, Q.; Sutter, E.; Sutter, P. Van der Waals heterostructures. *Nat. Rev. Methods Primers* **2022**, *2*, 58.

(36) Drouin, D.; Couture, A. R.; Joly, D.; Tastet, X.; Aimez, V.; Gauvin, R. CASINO V2.42 — A fast and easy-to-use modeling tool for scanning electron microscopy and microanalysis users. *Scanning* **2007**, *29*, 92–101.

(37) Evoy, S.; Harnett, C. K.; Keller, S.; Mishra, U. K.; DenBaars, S. P.; Craighead, H. G. Scanning tunneling microscope-induced luminescence studies of defects in GaN layers and heterostructures. *MRS Online Proceedings Library* **1999**, *588*, 19.

(38) Jahn, U.; Kaganer, V. M.; Sabelfeld, K. K.; Kireeva, A. E.; Lähnemann, J.; Pfüller, C.; Flissikowski, T.; Chèze, C.; Biermann, K.; Calarco, R.; Brandt, O. Carrier diffusion in GaN: A cathodoluminescence study. I. Temperature-dependent generation volume. *Phys. Rev. Appl.* **2022**, *17*, 024017.

(39) Guthrey, H.; Moseley, J. A review and perspective on cathodoluminescence analysis of halide perovskites. *Adv. Energy Mater.* **2020**, *10*, 1903840.

(40) Brunner, D.; Angerer, H.; Bustarret, E.; Freudenberg, F.; Höpler, R.; Dimitrov, R.; Ambacher, O.; Stutzmann, M. Optical constants of epitaxial AlGaN films and their temperature dependence. *J. Appl. Phys.* **1997**, *82*, 5090–5096.

(41) Podlipskas, Z.; Jurkevičius, J.; Kadys, A.; Miasojedovas, S.; Malinauskas, T.; Aleksiejūnas, R. The detrimental effect of AlGaN barrier quality on carrier dynamics in AlGaN/GaN interface. *Sci. Rep.* **2019**, *9*, 17346.

(42) Liu, W. *Ultrafast carrier dynamics in III-nitride nanostructures and LED quantum efficiency*; Ph.D. Dissertation, École Polytechnique Fédérale de Lausanne, Lausanne, Switzerland, 2019.

(43) Reshchikov, M. A.; Shahedipour, F.; Korotkov, R. Y.; Wessels, B. W.; Ulmer, M. P. Photoluminescence band near 2.9 eV in undoped GaN epitaxial layers. *J. Appl. Phys.* **2000**, *87*, 3351–3354.

(44) Birner, S.; Zibold, T.; Andlauer, T.; Kubis, T.; Sabathil, M.; Trellakis, A.; Vogl, P. nextnano: General purpose 3-D simulations. *IEEE Trans. Electron Devices* **2007**, *54*, 2137–2142.

(45) Rosencher, E.; Vinter, B. *Optoelectronics*; Cambridge University Press: Cambridge, UK, 2002.

(46) Vurgaftman, I.; Meyer, J. R. Band parameters for nitrogen-containing semiconductors. *J. Appl. Phys.* **2003**, *94*, 3675–3696.

(47) Nath, D. N.; Yang, Z. C.; Lee, C.-Y.; Park, P. S.; Wu, Y.-R.; Rajan, S. Unipolar vertical transport in GaN/AlGaN/GaN heterostructures. *Appl. Phys. Lett.* **2013**, *103*, 022102.

(48) Li, C.-K.; Piccardo, M.; Lu, L.-S.; Mayboroda, S.; Martinelli, L.; Peretti, J.; Speck, J. S.; Weisbuch, C.; Filoche, M.; Wu, Y.-R. Localization landscape theory of disorder in semicon-

ductors. III. Application to carrier transport and recombination in light emitting diodes. *Phys. Rev. B* **2017**, *95*, 144206.

(49) Triviño, N. V.; Butté, R.; Carlin, J.-F.; Grandjean, N. Continuous wave blue lasing in III-nitride nanobeam cavity on silicon. *Nano Lett.* **2015**, *15*, 1259–1263.

(50) Benameur, M. M.; Radisavljevic, B.; Héron, J. S.; Sahoo, S.; Berger, H.; Kis, A. Visibility of dichalcogenide nanolayers. *Nanotechnology* **2011**, *22*, 125706.

(51) Lee, C.; Yan, H.; Brus, L. E.; Heinz, T. F.; Hone, J.; Ryu, S. Anomalous lattice vibrations of single- and few-layer MoS_2. *ACS Nano* **2010**, *4*, 2695–2700.

(52) Nemes-Incze, P.; Osváth, Z.; Kamarás, K.; Biró, L. P. Anomalies in thickness measurements of graphene and few layer graphite crystals by tapping mode atomic force microscopy. *Carbon* **2008**, *46*, 1435–1442.

(53) Li, H.; Zhang, Q.; Yap, C. C. R.; Tay, B. K.; Edwin, T. H. T.; Olivier, A.; Baillargeat, D. From bulk to monolayer MoS_2: Evolution of Raman scattering. *Adv. Funct. Mater.* **2012**, *22*, 1385–1390.

(54) Buscema, M.; Steele, G. A.; van der Zant, H. S. J.; Castellanos-Gomez, A. The effect of the substrate on the Raman and photoluminescence emission of single-layer MoS_2. *Nano Res.* **2014**, *7*, 561–571.

(55) de la Peña, F. et al. hyperspy/hyperspy: Release v1.7.3. 2022; https://doi.org/10.5281/zenodo.7263263.